ALGORITHM THEORETICAL BASIS DOCUMENT

GOME-2 Total Column Products of Ozone, NO$_2$, BrO, HCHO, SO$_2$, H$_2$O, OClO and Cloud Properties

(GDP 4.8 for AC SAF OTO and NTO)

Prepared by: Pieter Valks   German Aerospace Center

Deutsches Zentrum für Luft und Raumfahrt e.V. – DLR
Oberpfaffenhofen, Germany

Signatures

Action: Name	Affiliation	Function	Date	Sign.
prepared by: P. Valks D. Loyola N. Hao P. Hedelt S. Slijkhuis M. Grossi S. Gimeno Garcia R. Lutz	DLR-MF DLR-MF DLR-MF DLR-MF DLR-MF DLR-MF DLR-MF DLR-MF	AC SAF Project Manager GOME Team Leader GOME Project Scientist GOME Project Scientist GOME Project Scientist GOME Project Scientist GOME Project Scientist GOME Project Scientist	27.06.2017	
released by: P. Valks	DLR-MF	AC SAF Project Manager	27.06.2017	

Distribution List

Function	Organization
GOME/GDP Team	DLR-MF, DLR-DFD
AC SAF Team	EUMETSAT, FMI, KNMI, DMI, BIRA, AUTH, various

Document Change Log

Issue	Rev.	Date	Section	Description of Change
1/A	1	4 May 2007	All	Completely new
1/B	1	12 Oct. 2007	All	Revised following ORR-A
1/C	1	14 April 2008	3, 4	Update tropospheric NO_2 and BrO algorithms
2/A	1	17 Nov. 2008 28 Jan. 2009	All	Revisions following ORR-A3 Harmonise with PUM
2/B	1	03 Mar. 2009 14 April 2009 30 Oct. 2009	6,9 4 6	H_2O algorithm added BrO algorithm updated H_2O algorithm updated
2/C	1	30 Jan. 2010 19 Feb. 2010 14 May 2010	6 2.5 2.4 2.5	H_2O algorithm updated Scan angle correction updated Molecular Ring correction Empirical Correction for scan angle dependency
2/D	1	10 Jan. 2011	6	H_2O algorithm updated (albedo database)
2/E	1	23 Mar. 2011	All 6	Version update from GDP 4.4 to GDP 4.5 Description and reference for H_2O cloud flag added
2/F	1	14 April 2011	6	Reference for albedo correction Update of error calculation for total column H_2O
2/G	1	16 Feb 2012	9	Tropospheric O_3 algorithm added
2/H	1	21 May 2013	All 2	GOME-2 / MetOp-B included O_3 algorithm updated

			4	BrO algorithm updated
			5	SO_2 algorithm updated
			6	H_2O algorithm updated
3/A	1	15 Oct. 2016	All	ATBD restructured Tropical tropospheric ozone chapter moved to separate ATDB Algorithm descriptions improved and updated to GDP 4.8
3/A	2	27 June 2017	All	OCIO chapter included Change SAF naming to AC SAF

TABLE OF CONTENTS

EUMETSAT SATELLITE APPLICATION FACILITY ON ATMOSPHERIC COMPOSITION MONITORING (AC SAF)

Background

The need for atmospheric composition monitoring was first realized when severe loss of stratospheric ozone was detected over the Polar Regions. At the same time, increased levels of ultraviolet radiation were observed.

Ultraviolet radiation is known to be dangerous to humans and animals (causing e.g. skin cancer, cataract, immune suppression) and having harmful effects on agriculture, forests and oceanic food chain. In addition, the global warming - besides affecting the atmospheric chemistry - also enhances the ozone depletion by cooling the stratosphere. Combined, these phenomena have immense effects on the whole planet. Therefore, monitoring the chemical composition of the atmosphere is a very important duty for EUMETSAT and the world-wide scientific community.

Objective

The main objectives of the AC SAF is to process, archive, validate and disseminate atmospheric composition products (O_3, NO_2, SO_2, BrO, HCHO, H_2O and OClO), aerosol products and surface ultraviolet radiation products utilising the satellites of EUMETSAT. The majority of the AC SAF products are based on data from the GOME-2 spectrometers onboard Metop-A and Metop-B satellites. Another important task of the AC SAF is the research and development in radiative transfer modelling and inversion methods for obtaining long-term, high-quality atmospheric composition products from the satellite measurements.

Product categories, timeliness and dissemination

Data products are divided in two categories depending on how quickly they are available to users:
Near real-time products are available in less than three hours after measurement. These products are disseminated via EUMETCast, WMO GTS or internet.

- Near real-time trace gas columns
  - O_3, NO_2, HCHO, SO_2
- Near real-time ozone profiles
  - coarse and high-resolution
- Near real-time absorbing aerosol indexes
  - from main science channels and polarization measurement detectors
- Near real-time UV indexes
  - clear-sky and cloud-corrected

Offline products are available in two weeks after measurement and disseminated via dedicated web services at EUMETSAT, FMI and DLR.

- Offline trace gas columns
  - O_3, NO_2, SO_2, BrO, HCHO, H_2O and OClO
- Offline ozone profiles
  - coarse and high-resolution
- Offline absorbing aerosol indexes
  - from main science channels and polarization measurement detectors
- Offline surface UV

More information about the AC SAF project, products and services: http://acsaf.org/
AC SAF Helpdesk: helpdesk@acsaf.org

1   INTRODUCTION

1.1 Purpose and scope

This document describes the GOME-2 Data Processor Version 4.8 (GDP 4.8), the operational algorithm for the retrieval of total columns of trace gases from the GOME-2 instruments on MetOp-A and MetOp-B, as part of the AC SAF. GDP 4.8 is based on DOAS-style algorithms, originally developed for GOME/ERS-2 (e.g. Spurr et al., 2004).

This document contains descriptions of the trace gas column and cloud retrieval algorithms for GOME-2. The product format and dissemination information are given in the corresponding Product User Manual (Valks et al., 2017). Validation results of the GOME-2 total ozone, NO_2, BrO, HCHO, SO_2, H_2O and OClO columns with ground-based measurements are described in the AC SAF Validation Reports (Balis et al., 2013; De Smedt et al., 2013, 2015; Grossi et al., 2015; Kalakoski et al., 2013, 2014; Koukouli et al., 2012, 2015; Lambert et al., 2011; Pinardi et al., 2013, 2015, 2017; Theys et al., 2013a, 2013b, 2015a, 2015b).

In this document, the terms GOME/ERS-2, GOME-2/MetOp-A and GOME-2/MetOp-B are used to reference the specific instruments. The term GOME-2 applies to both GOME-2 instruments on MetOp-A and -B.

1.2 MetOp and GOME-2

On 30 January 1998, the ESA Earth Observation Programme Board gave its final go-ahead for the MetOp Programme. The instruments on the MetOp satellites produce high-resolution images of the Earth's surface, vertical temperature and humidity profiles, and temperatures of the land and ocean surface on a global basis. In addition, there are instruments for monitoring ozone and other key trace gases in the troposphere and stratosphere, and for measuring the wind flow over the oceans.

Given the need for global-scale routine monitoring of the abundance and distribution of ozone and associated trace gas species, a proposal was put forward for the inclusion of GOME-2 on the MetOp satellites. MetOp-A was launched on 19 October 2006 as part of the Initial Joint Polar System (IJPS) in co-operation with NOAA in the USA. The second polar-orbiting satellite in the series, MetOp-B, was successfully launched on 17 September 2012. MetOp-A and MetOp-B are flying on a sun-synchronous orbit with a repeat cycle of 29 days and an equator crossing time of 09:30 LT (descending mode).

GOME-2 is a nadir-scanning UV-VIS spectrometer (Munro et al., 2006), covering the spectral range between 240 and 790 nm with a spectral resolution between 0.26 nm and 0.51 nm (FWHM). Additionally, two polarisation components are measured with polarisation measurement devices (PMDs) at 30 broad-band channels covering the full spectral range. The default swath width of the GOME-2 scan is 1920 km, which enables global coverage in about 1.5 days. GOME-2 ground pixels have a default footprint size of 80×40 km^2 in the forward scan, which is four times smaller than those for GOME (320×40 km^2), but larger than those for SCIAMACHY (30×60 km^2) and OMI (24×13 km^2 at nadir). Owing to a non-linear movement of the scan mirror, the ground pixel size remains nearly constant over the full scan. In the tandem mode, GOME-2/Metop-A operates on a reduced swath width of 960 km with an increased spatial resolution (approx. 40×40 km^2), while GOME-2/Metop-B operates on a nominal wide swath at 1920 km. This implementation increases both the daily coverage and the spatial resolution of GOME-2 measurements. GOME-2 tandem operations started on 15 July 2013.

Based on the successful work with the GOME data processors, the German Aerospace Centre (DLR) plays a major role in the design, implementation and operation of the GOME-2 ground segment for the trace gas column products. DLR is a partner in the Satellite Application Facility on Atmospheric Composition Monitoring (AC SAF), which is part of the EUMETSAT Polar System (EPS) ground segment, and is responsible in this project for the generation of total column amounts of the various trace gases and cloud properties which may be retrieved from GOME-2 level 1b products.

1.3 Overview of the GDP 4.8 algorithm

The operational GOME-2 trace gas column products from MetOp-A and MetOp-B are generated at the DLR using the UPAS (Universal Processor for UV/VIS Atmospheric Spectrometers) environment version 1.3.9 implementing the level-1-to-2 GOME Data Processor (GDP) 4.8 algorithm.

1.3.1   DOAS-AMF algorithm

The GDP 4.8 is a classical DOAS-AMF fitting algorithm for the retrieval of total column amounts of ozone, NO_2, BrO, HCHO, SO_2 and H_2O (Van Roozendael et al., 2006; Loyola et al., 2011, Valks et al., 2011; Hao et al., 2014; Grossi et al., 2015). The algorithm has two major steps: a DOAS least-squares fitting for the trace gas slant column density (SCD), followed by the computation of a suitable Air Mass Factor (AMF) to make the conversion to the vertical column density (VCD). Figure 1 is a schematic flowchart for the GDP 4.8 trace-gas column algorithm (including some specific ozone retrieval steps). In a pre-processing step, cloud information (fractional cover, cloud-top height and cloud albedo) is derived before the above two major algorithm components are executed. The GDP 4.8 is also used to retrieve OClO columns from GOME-2. However, OClO can only be observed at very low sun, around solar zenith angles of 90°, and therefore the GOME-2 data product only contain slant columns of OClO (see Chap. 8). In GDP 4.8, cloud parameters are computed directly by calls to the OCRA/ROCINN algorithms (Loyola, 2004, 2007; Lutz et al., 2016), see Chap. 9.

The first major algorithm component in the GDP is the DOAS fitting. This is a straightforward least-squares inversion to deliver the effective slant column of the trace gas of interest, plus a number of auxiliary fitted parameters and error diagnostics. The latter include slant columns of interfering species in the wavelength window, a scaling factor for interference due to the Ring effect, wavelength registration parameters, and low-pass filter closure parameters (see Sect. 2.2). Table 1 lists the wavelength regions used for the retrieval of the trace gas column and cloud products with the GDP 4.8.

The second major component is the AMF calculation in order to generate the final trace gas vertical column (VCD = SCD / AMF). The AMF is computed using a radiative transfer model, and depends on the (*a priori*) vertical trace gas profile, the GOME-2 viewing geometry, the surface albedo and altitude, as well as on clouds and aerosols (e.g. see Sect. 2.3 and 3.2). The accuracy of the AMF is mostly limited by the current knowledge on these external parameters. For tropospheric trace gases such as NO_2 and HCHO, the dependence of the AMF on the *a priori* trace gas profile, surface albedo, cloud and aerosols is much stronger than for stratospheric trace gases (e.g. ozone), and this introduces an important error source in the retrieval of the trace gas vertical column. For example, the estimation of the AMF introduces the largest error source in the retrieval of the tropospheric NO_2 column under polluted conditions (see Sect. 3.4).

Table 1   GOME-2 trace gas column and cloud products generated with the GDP 4.8, with the corresponding wavelength regions used for the retrieval.

Product	Wavelength region
Ozone column	325.0-335.0 nm
NO_2 column	425.0-450.0 nm
BrO column	332.0-359.0 nm
HCHO column	328.5-346.0 nm
SO_2 column	315.0-326.0 nm
H_2O column	614.0-683.2 nm
OClO column	345.0-389.0 nm
cloud fraction	300-800 nm (PMD-p)
cloud-top height (pressure) & albedo (optical thickness)	758-771 nm
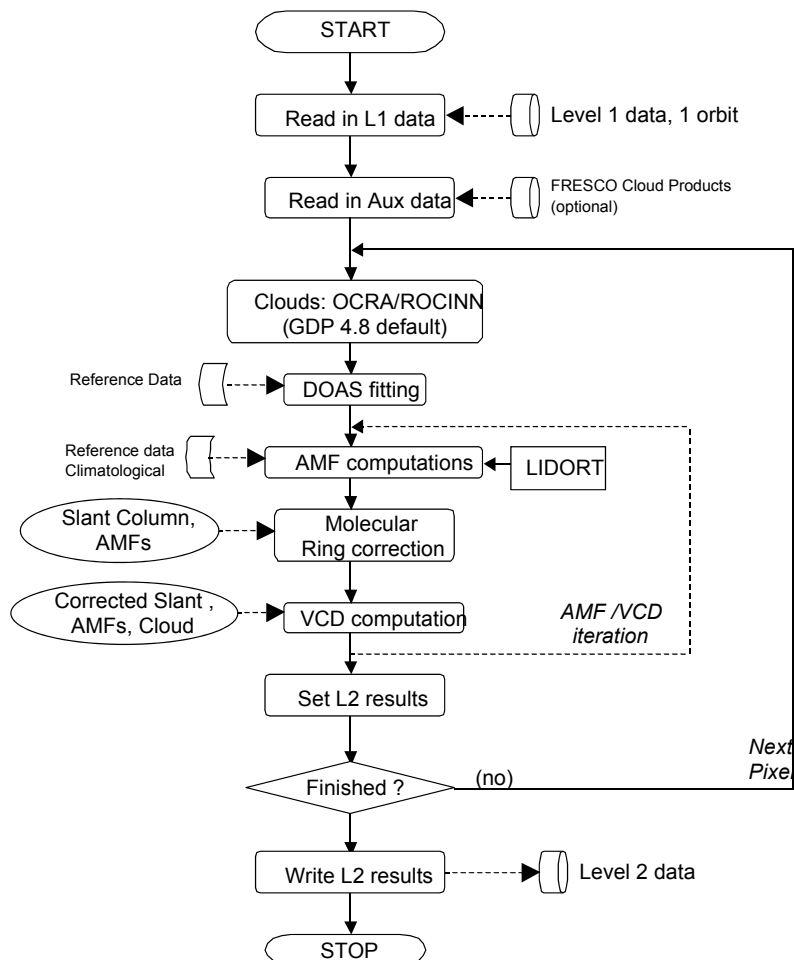
Figure 1 Flow diagram of the GDP 4.8 trace gas column algorithm for GOME-2 (adapted from Van Roozendael et al. (2006)). The molecular Ring correction and AMF/VCD iteration are specific ozone retrieval steps.

1.3.2 Main algorithm improvements in the GDP 4.8

The main changes in the GDP 4.8 algorithm (compared to the previous version 4.7) for the different GOME-2 trace gas column and cloud products is summarizes in Table 2.

1.4 Document overview

In the next chapter, the ozone column algorithm is described. A general description of the DOAS slant column algorithm is given, and the vertical ozone column calculation using the Air Mass Factor is described. The ozone column error budgets and sensitivity studies are addressed as well. In the following chapters, specific retrieval algorithm aspects for the NO_2, BrO, HCHO, SO_2, H_2O and OClO column products are described. A description of the GOME-2 cloud algorithms OCRA and ROCINN is provided in Chap. 9.

	REFERENCE:	**SAF/AC/DLR/ATBD/01**
	ISSUE:	3/A	Rev. 2
	DATE:	27.06.2017
	PAGE:	12

EUMETSAT
AC SAF
ATMOSPHERIC COMPOSITION
MONITORING

Table 2   Main changes in the GDP 4.8 algorithm (compared to the previous version 4.7) for the different GOME-2 trace gas column and cloud products.

Product	GDP 4.8 algorithm improvements
Ozone column	Improved correction for the scan angle dependency, see Sect.2.5. Flagging of ozone columns with strong SO_2 absorption interference (volcanic eruptions), see Sect. 2.6.1
NO_2 column	Updated NO_2 absorption cross-sections (Vandaele et al., 2002), see Sect. 3.1.
HCHO column	Two-step DOAS fit retrieval method, see Sect. 5.1. Provision of Averaging Kernels, see Sect. 5.3.
SO_2 column	Improved DOAS settings, see Sect. 6.1. Additional SO_2 column retrieval for anthropogenic emission scenario. New algorithm for volcano activity detection, see Sect. 6.4
H_2O column	Improved correction for the scan angel dependency, see Sect. 7.4.
OClO column	New product, see Chap. 8
Cloud fraction (OCRA)	Empirical degradation correction based on PMD data. Improved sun-glint detection and correction, see Sect. 9.1.
Cloud-top height & albedo (ROCINN)	Degradation corrections for O2 A-band New inversion scheme (Tikhonov regularization), see Sect. 9.2

1.5 Abbreviations and acronyms

A list of abbreviations and acronyms which are used throughout this document is given below:

AC SAF	EUMETSAT Satellite Application Facility on Atmospheric Composition Monitoring
AMF	Air Mass Factor
BIRA-IASB	Belgian Institute for Space Aeronomy
DLR	Deutsches Zentrum für Luft- und Raumfahrt e.V. (German Aerospace Centre)
DOAS	Differential Optical Absorption Spectroscopy
DU	Dobson Unit
EPS	EUMETSAT Polar System
ERS-2	European Remote Sensing Satellite-2
ESA	European Space Agency
ESC	Effective Slant Column
EUMETSAT	European Organisation for the Exploitation of Meteorological Satellites
GDOAS	GODFIT-DOAS
GDP	GOME Data Processor
GOME	Global Ozone Monitoring Experiment
LER	Lambertian Equivalent Reflectivity
LIDORT	Linearized Discrete Ordinate Radiative Transfer Forward Modeling
MetOp	Operational Meteorological Satellite
NRT	Near Real Time
NTO	Identifier used for near-real-time total column trace gas products
OCRA	Optical Cloud Recognition Algorithm
OL	Off-line
OTO	Identifier used for offline total column trace gas products
P-S	Pseudo-Spherical
PMD	Polarisation Measurement Device
RMS	Root Mean Square
ROCINN	Retrieval of Cloud Information using Neural Networks
RRS	Rotational Raman Scattering
RT	Radiative Transfer
SAF	Satellite Application Facility
SCD	Slant Column Density
SZA	Solar Zenith Angle
TOA	Top of Atmosphere
TOMS	Total Ozone Mapping Spectrometer
UMARF	Unified Meteorological Archiving and Retrieval Facility
UV	Ultra Violet
UPAS	Universal Processor for UV/VIS Atmospheric Spectrometers
UTC	Universal Time Coordinate
VCD	Vertical Column Density
VIS	Visible

2 THE OZONE COLUMN ALGORITHM

2.1 Introduction

The first major algorithm component is the DOAS fitting to deliver the effective slant column of total ozone, plus a number of auxiliary fitted parameters and error diagnostics. The latter include an effective temperature for the ozone absorption, a slant column for NO_2 (regarded as an interfering species in the ozone UV window), wavelength registration parameters for re-sampling the earthshine spectrum, scaling factors for interference due to undersampling and Ring effects, and low-pass filter closure parameters.

The second major component is the iterative AMF/VCD (Air Mass Factor, Vertical Column Density) computation to generate the final vertical column. An initial guess is made for the VCD. At each iteration step, ozone air mass factors (to ground level and to cloud-top) are computed for the current guess of the vertical column. This radiative transfer calculation uses a column-classified ozone profile climatology. Then the DOAS slant column is adjusted using the molecular Ring correction (to compensate for interference effects in ozone absorption features due to inelastic rotational Raman scattering). This adjusted slant column is then used in conjunction with pre-processed cloud information and the AMF values to update the VCD guess. The processing is completed by writing a Level 2 output file (total column, errors and retrieval diagnostics, and auxiliary output such as surface pressure and selected Level 1 geolocation information) for one orbit of data.

The ozone column algorithm components are described in the next sections (see also Loyola et al. (2011) and Hao et al., (2014)), starting with the DOAS fitting (Sect. 2.2), moving on to the iterative AMF/VCD computation (Sect. 2.3), and the molecular Ring correction (Sect. 2.4). An empirical correction for the scan angle dependency in the GOME-2 ozone columns is described in Sect. 2.5. In Sect. 2.6, we present an error budget for the total ozone algorithm, and discuss a number of sensitivity tests.

2.2 DOAS slant column fitting

In DOAS fitting, the basic model is the Beer-Lambert extinction law for trace gas absorbers (Spurr et al., 2005). An external polynomial closure term accounts for broadband effects: molecular scattering, aerosol scattering and absorption and reflection from the Earth's surface. We also include additive spectra for Ring effect interference. The fitting model is then:

$$Y(\lambda) \equiv \ln\left[\frac{I_\lambda(\Theta)}{I_\lambda^0(\Theta)}\right] = -\sum_g S_g(\Theta)\sigma_g(\lambda) - \sum_{j=0}^{3}\alpha_j\left(\lambda - \lambda^*\right)^j - \alpha_R R(\lambda) \tag{1}$$

Here, I_λ is the earthshine spectrum at wavelength λ, I_λ^0 the solar spectrum, $S_g(\Theta)$ the effective slant column density of gas g along geometrical path Θ, $\sigma_g(\lambda)$ is the associated trace gas absorption cross section. The second term in Eq. (1) is the closure polynomial (a cubic filter has been assumed), with λ^* a reference wavelength for this polynomial. The last term on the right hand side of Eq. (1) is the additive terms for the Ring reference spectrum $R(\lambda)$. The fitting minimizes the weighted least squares difference between measured and simulated optical densities $Y_{meas}(\lambda)$ and $Y_{sim}(\lambda)$ respectively. The model in Eq. (1) is linear in the slant columns $S_g(\Theta)$, the polynomial coefficients $\{\alpha_k\}$ and the Ring scaling parameters α_R.

Shift and squeeze parameters may be applied to cross-section wavelength grids to improve wavelength registration against Level 1 spectra. Experience with DOAS in the operational GDP processor has shown that fitting of such non-linear parameters on a pixel-by-pixel basis can sometimes leads to numerical instability, and an optimized pre-shift value needs to be applied. Furthermore, it was found that DOAS fitting for GOME total columns achieves greater accuracy when

two ozone cross-sections at different temperatures are used as reference spectra (Richter and Burrows, 2002). For GOME-2/MetOp-A, we used re-convolved GOME-FM98 ozone cross-sections (i.e. de-convolved GOME-FM98 ozone cross-sections (Burrows et al., 1999b), convolved with the GOME-2 FM3 slit function v1.1 (Siddans et al., 2006)) in the DOAS ozone slant column retrieval (GDP 4.6 and earlier versions), because of the poor quality of original GOME-2 FM3 ozone cross section data. Recently, updated GOME-2 FM3 ozone cross section data have been released (Chehade et al., 2013).

In principle, the retrieval should be independent of the choice of the cross sections temperatures selected for use in the DOAS fitting procedure. The behavior of the GOME-FM98 (reconvolved with the GOME-2 slit function), the updated GOME-2 FM3 and the Brion/Malicet ozone cross-section data set (Malicet et al., 1995; Brion et al., 1998) has been analysed from this point of view. Four parameters have been used for the analysis: the RMS, the percent change in O_3 slant column relative to the column obtained using GOME-FM98 241-221K combination (GDP 4.6 settings), the retrieved effective temperature and the O_3 cross section wavelength shift. Results (see Fig. 2) obtained with the GOME-FM98 and Brion/Malicet cross-sections show stability in the sense that the values retrieved for each test parameter are independent of the cross section temperature selected for processing. In contrast, results obtained with the GOME-2 FM3 cross-sections show a much larger variability. Difference in O_3 slant columns as large as 4% can be obtained depending on the combination of cross sections selected for retrieval, mostly as a result of the instability in the derived temperatures. The GOME-2 O_3 slant column densities retrieved using Brion/Malicet cross-sections are about 3% larger than using GOME-FM98 cross sections. Considering the low bias in the GOME-2 ozone columns retrieved with the GDP 4.6 compared to ground-based measurements (Balis et al., 2009; Loyola et al., 2011), Brion/Malicet cross sections at 243K and 218K are used for the GOME-2 ozone column retrieval since the GDP 4.7 for both MetOp-A and MetOp-B (Hao et al. 2014).
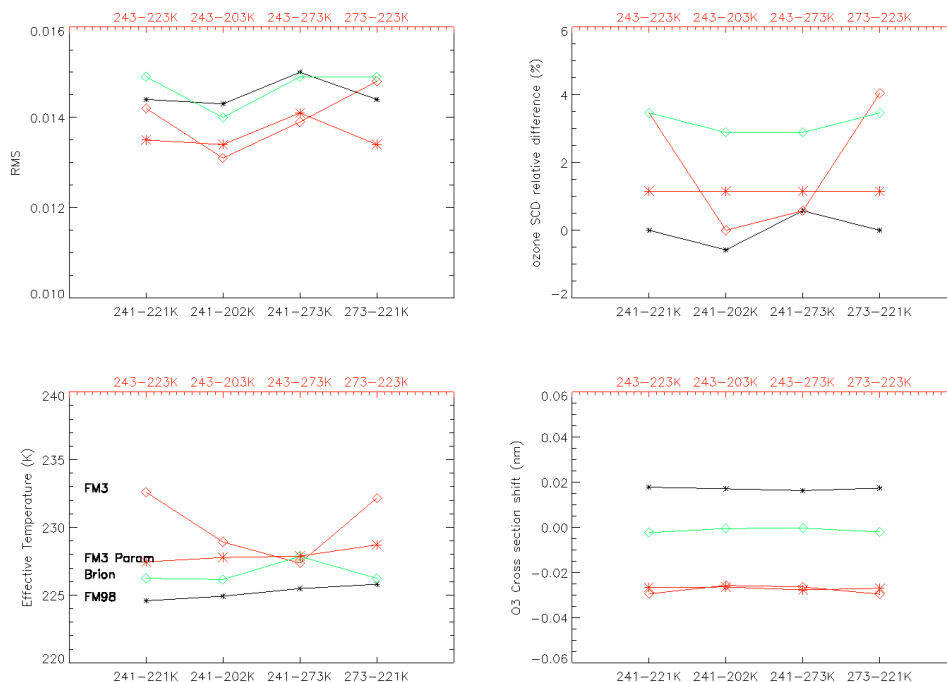

Figure 2   RMS fit residuals, O_3 slant column relative differences, effective temperatures and O_3 cross section wavelength shift from the DOAS ozone retrieval for pixel #8500 of GOME-2/MetOp-Orbit 20392, using different combinations of O_3 absorption cross-section data sets.

Pre-shifting of the ozone and NO_2 cross-sections is required to compensate for inaccuracies in the wavelength calibration of the cross-section data. The convolved Brion/Malicet ozone cross-sections require a pre-shift of -0.004 nm and are corrected for the so-called I_0 effect (Aliwell et al., 2002).

In the GDP, the solar spectrum is used as the wavelength reference. Shift and squeeze parameters are applied to each Earthshine wavelength grid in order to re-sample the Earthshine spectrum. If necessary, the wavelength calibration of the GOME-2 level-1 spectra can be improved by applying window-dependent pre-shifts to parts of the solar spectrum before each orbit of data is processed. These pre-shifts are established by cross-correlation with a high-resolution solar spectrum (Chance and Kurucz, 2010) over limited wavelength ranges covering the fitting window (325-335 nm for O_3). For GOME-2 a relatively small pre-shift is found for the ozone fitting window (0.001 nm for GOME-2/MetOp-A and 0.006 nm for GOME-2/MetOp-B).

The Ring effect (filling-in of well-modulated solar and absorption features in earthshine spectra) is due to inelastic rotational Raman scattering (RRS). In DOAS fitting, it is treated as an additional absorber, by means of an additive Ring reference spectrum and associated scaling parameter, as in Eq. (1) above. The simplest 'Fraunhofer' Ring spectrum is obtained by folding rotational Raman cross-sections at a fixed temperature with a high-resolution Fraunhofer spectrum taken from the Kitt Peak Observatory (Chance and Kurucz, 2010), but this does not include a telluric contribution. In the UV window 325-335 nm, Ring effect distortion of O_3 Huggins bands absorption features is large enough to seriously compromise total ozone fitting accuracy. As noted already, a molecular Ring effect correction was developed for GOME total ozone (Van Roozendael et al., 2006), that is used for the GOME-2 ozone retrieval in the GDP 4.8. This correction is an *ex post facto* scaling of the DOAS slant column result, and it is performed at each iteration step in the AMF/VCD calculations (see Sect. 2.3). A description of this molecular Ring correction algorithm is presented in Sect. 2.4.

The DOAS state vector for linear fitting in GDP 4.8 has 9 parameters: 2 effective slant columns of O_3 and NO_2, 1 fitting parameter for a second O_3 cross-section (to derive the effective temperature T_{eff}), 4 closure coefficients, and 2 additive scaling factors (corresponding to Fraunhofer Ring and undersampling reference spectra). There are 2 parameters in the nonlinear least-squares fitting: a wavelength shift and squeeze for re-sampling the earthshine spectrum on to the solar spectrum reference wavelength grid.

2.3 Air Mass Factor and vertical column computations

2.3.1 Iterative AMF/VCD method

The definition of the Air Mass Factor *M* used in the GDP is the traditional one:

$$M = \frac{\log(I_{nog} / I_g)}{\tau_{vert}} , \qquad (2)$$

where I_g is the radiance for an atmosphere including the particular trace gas as an absorber, I_{nog} is the radiance for an atmosphere without this trace gas and τ_{vert} is the vertical optical thickness of the trace gas.

To simulate the backscatter radiances I_g and I_{nog} in the AMF definition (Eq. (2)), the LIDORT radiative transfer model is used (Spurr et al., 2001). LIDORT is a multiple scatter multi-layer discrete ordinate radiative transfer code. The atmosphere is assumed stratified into a number of optically uniform layers. The LIDORT code used here neglects light polarization. Although polarization in RT simulations is an important consideration for ozone profile algorithms, in DOAS retrievals with narrow fitting windows in the UV, the polarization signature is subsumed in the closure polynomial. We use the LIDORT Version 3.7 (Spurr, 2003, 2008) which possesses corrections for beam attenuation along curved line-of-sight paths, needed for the wide viewing angles of GOME-2 (scan angles in the range 40-50°)

For GOME-2 scenarios, computation of the vertical column density V proceeds via the relation:

$$V = \frac{S + wGM_{cloud}}{(1-w)M_{clear} + wM_{cloud}},$$ (3)

where S is the DOAS-retrieved slant column, M_{clear} the clear sky AMF, M_{cloud} the AMF for the atmosphere down to the cloud-top level, and the "ghost column" G is the quantity of ozone below the cloud-top height, which cannot be detected by GOME-2 and is derived from an ozone profile climatology (see Sect. 2.3.2). This formula assumes the independent pixel approximation for cloud treatment. In the GDP, we use the "intensity-weighted cloud fraction" w defined as:

$$w = \frac{c_f I_{cloud}}{(1-c_f)I_{clear} + c_f I_{cloud}},$$ (4)

where I_{clear} and I_{cloud} are the backscattered radiances for cloud-free and cloud-covered scenes respectively. I_{clear} and I_{cloud} are calculated with the LIDORT radiative transfer model, and depend mainly on the surface and cloud albedos and on the GOME-2 viewing geometry.

AMFs depend on ozone profiles through the radiative transfer model. In traditional DOAS retrievals, the ozone AMF depends on a fixed ozone profile taken from climatology; one application of Eq. (3) yields the VCD. In the iterative approach to AMF calculation, we use a column-classified ozone profile climatology to establish a unique relationship between the ozone profile and its corresponding total column amount. The AMF values are now considered to be functions of the VCD through this profile-column relation, and the above formula in Eq. (3) is used to update the VCD value according to:

$$V^{(n+1)} = \frac{S + wG^{(n)}M_{cloud}^{(n)}}{(1-w)M_{clear}^{(n)} + wM_{cloud}^{(n)}}$$ (5)

Here, the (n) superscript indicates the iteration number. The AMFs $M_{clear}^{(n)}$ and $M_{cloud}^{(n)}$, and the ghost column $G^{(n)}$, depend on the value of the vertical column $V^{(n)}$ at the nth iteration step. In this iteration, the slant column S reflects the true state of the atmosphere and acts as a constraint on the iteration. Equation (5) is applied repeatedly until the relative change in $V^{(n)}$ is less than a prescribed small number ε. In other words, convergence is reached when $|(V_{n+1}/V_n) - 1| < \varepsilon$. For a value of ε set at 10^{-4} (the GDP 4.8 operational baseline), convergence is rapid and 3-5 iterations are usually sufficient. The first guess choice V^0 comes from a zonally-averaged total column climatology derived from many years of TOMS data (see next section).

In GDP 4.8, there is a molecular Ring correction C_{Ring} applied to the slant column S, and we must therefore use a corrected slant column $S_{corr} = S/C_{Ring}$ in the iteration. As we will see in Sect. 2.4, C_{Ring} depends on the total AMF, defined to be $M_{total} = (1-w)M_{clear} + wM_{cloud}$. Clearly C_{Ring} will need to be updated at each AMF/VCD iteration step, and our iteration formula now reads:

$$V^{(n+1)} = \frac{\dfrac{S}{C_{Ring}^{(n)}} + wG^{(n)}M_{cloud}^{(n)}}{(1-w)M_{clear}^{(n)} + wM_{cloud}^{(n)}}.$$ (6)

The iterative AMF/VCD algorithm is straightforward to implement, and a flow diagram of the GDP application is shown in Fig. 3.

	REFERENCE:	**SAF/AC/DLR/ATBD/01**
	ISSUE:	3/A | Rev. 2
	DATE:	27.06.2017
	PAGE:	19

EUMETSAT
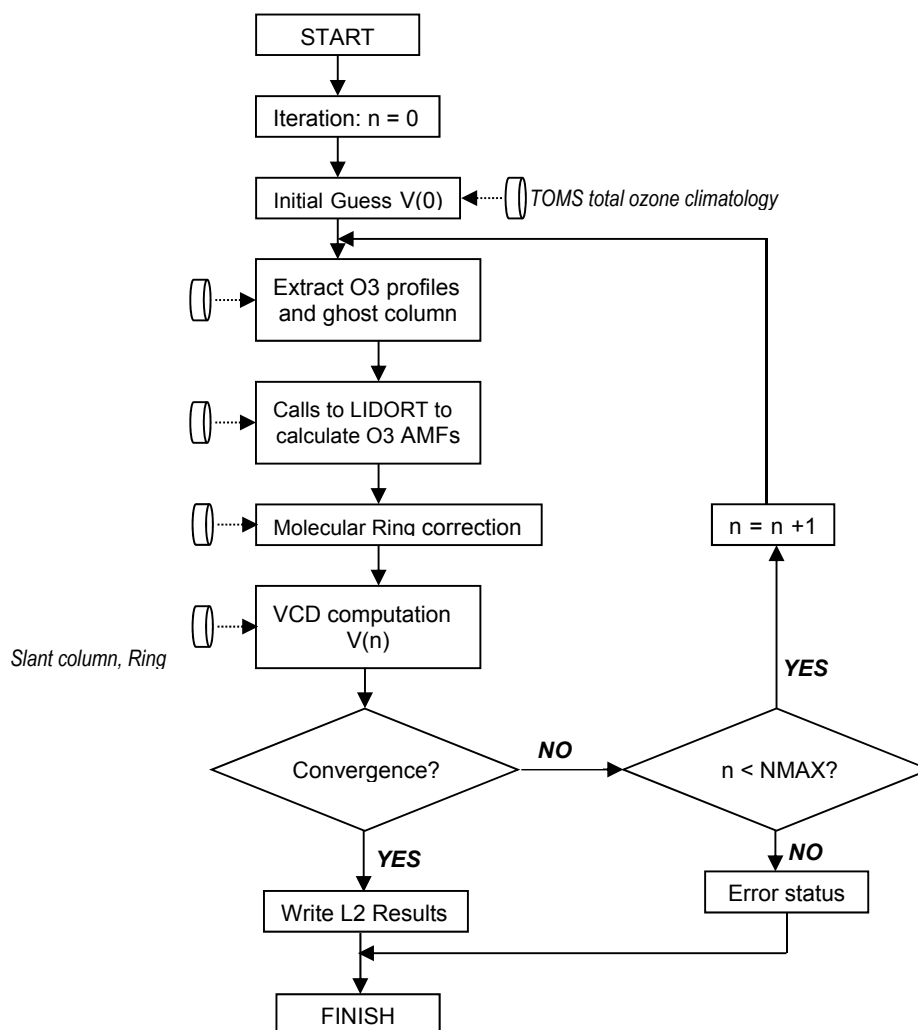**AC SAF**
ATMOSPHERIC COMPOSITION
MONITORING

Figure 3 Functional diagram of the iterative solution scheme for ozone air mass factors and vertical column densities in the GDP (adapted from Van Roozendael et al. (2006)).

2.3.2   The ozone profile-column map

A column-classified ozone profile climatology has been developed for TOMS Version 8 (Bhartia, 2003) and this climatology has been implemented for the GOME and GOME-2 total ozone retrieval in the GDP. The TV8 ozone profile climatology has a more sophisticated classification scheme than its predecessor, with 12 monthly profiles in 18 latitude zones at 10º intervals. The TV8 data has a variable column classification, from 3-5 columns at tropical latitudes and as much as 11 columns for polar regions. Column amounts vary from 125 DU to 575 DU and are separated at 50 DU intervals. Profile partial column amounts are also given in Dobson units.

The total ozone column V is the sum of the partial columns $\{U_j\}$ that make up a given ozone profile, where j is an index for the atmospheric layering. In the TV8 climatology, we are given a number of partial column profiles corresponding to fixed total column amounts. The profile-column mapping establishes the profile to be used for arbitrary values of the total column. For the linear profile-column map, the desired profile is expressed as a linear combination of two adjacent profiles $\{U_j^{(1)}\}$ and $\{U_j^{(2)}\}$ with corresponding total columns $V^{(1)}$ and $V^{(2)}$ bracketing V:

$$U_j(V) = \left(\frac{V - V^{(1)}}{V^{(2)} - V^{(1)}}\right)U_j^{(2)} + \left(\frac{V^{(2)} - V}{V^{(2)} - V^{(1)}}\right)U_j^{(1)}. \tag{7}$$

If the vertical column lies outside the range of values classifying the climatology, the profile is determined using a stable spline extrapolation scheme. This situation may occur in extreme ozone-hole scenarios (V < 125 DU). Latitude and time of GOME-2 measurements are specified from Level 1 geolocation information. In order to avoid jump artefacts associated with discrete latitude and time classifications, the climatological profiles are interpolated between latitude bands using a linear weighting scheme based on the cosine of the latitude, and over time using a linear weighting based on the day of the month.

In the GDP, we use the pressure grid of the ozone profile climatology for calculating layer optical properties required for the LIDORT computations. The TV8 climatology uses 11 partial columns with layer pressure differences based on atmospheric scale heights (pressures are halved for each successive atmospheric boundary). For each GOME-2 pixel, it is necessary to adjust the lowest-layer partial column to account for the actual surface pressure (this depends for the most part on the assigned topographical height). This adjustment is done by scaling the partial column with the logarithm of the layer pressure difference. For the computation of AMFs to cloud-top, the lowest layer is bounded by the cloud-top pressure, and the corresponding partial column will also scale with the logarithmic pressure drop. The ghost column is the difference between clear and cloudy sky total columns, and it emerges directly from the profile-column mapping.

2.3.3 Intra-Cloud correction

GDP 4.8 treats clouds as Lambertian surfaces, i.e. the scattering by cloud particles is modelled by a Lambertian Equivalent Reflectivity (LER). This cloud model is called Clouds as Reflecting Boundaries (CRB).The intra-cloud ozone column is improperly modeled in the LER approach, it may have a significant effect on the backscatter signal and total column errors could be large (Liu et al., 2004). The total column below cloud-top is actually the sum of the intra-cloud ozone column (V_{ic}) plus the column below the cloud itself. In reality, backscatter measurements are sensitive to V_{ic}, and the traditional LER methods will overestimate the total atmospheric column by ignoring V_{ic}. Therefore, the GDP 4.8 uses a simple correction called Semi-transparent Lambertian cloud (STLC) model (Loyola, 2007). It provides an initial empirical characterization of V_{ic} as function of the climatological ozone column below cloud-top (ghost column), the cloud albedo, and the solar zenith angle.

2.3.4 Radiative Transfer Model for the AMF calculation

In GDP 4.8, the AMFs are computed directly using a fast radiative transfer model that is able to deliver all necessary AMF results well within the data turn-over rate. The LIDORT radiative transfer model (Spurr et al., 2001, Spurr, 2008) is used to simulate backscatter radiances I_g and I_{nog} in the AMF definition in Eq. (2). LIDORT is a multiple scatter multi-layer discrete ordinate radiative transfer code. The atmosphere is assumed stratified into a number of optically uniform layers (in the ozone AMF computations, the layering scheme follows the TV8 pressure grid). The LIDORT code uses the pseudo-spherical (P-S) approximation: all scattering takes place in a plane-parallel medium, but attenuation of the solar beam before scatter is determined by ray-tracing through a spherical-shell atmosphere. The LIDORT code used here neglects light polarization. Although polarization in RT simulations is an important consideration for ozone profile algorithms, in DOAS retrievals with narrow fitting windows in the UV, the polarization signature is subsumed in the closure polynomial.
The P-S approximation is sufficiently accurate for AMF computations with solar zenith angle (SZA) up to 90° and for line-of-sight viewing angles up to 30-35° from the nadir. However, the P-S implementation is not accurate enough for the large viewing angles of GOME-2. This requires additional corrections for beam attenuation along curved line-of-sight paths, and for this we use the

LIDORT Version 3.7 (Spurr, 2003, 2008) which possesses this line-of-sight correction. LIDORT V3.7 is used for all viewing modes in order to maintain consistency.

For DOAS applications with optically thin absorbers, the trace gas AMF wavelength dependence is weak and it is customary to choose the mid-point wavelength of the fitting window. This does not apply to ozone in the 325-335 nm DOAS fitting window, and for GDP versions up to and including 3.0, the O_3 AMF was always calculated at 325.0 nm. The motivation and explanation for this choice of wavelength may be found in (Burrows et al., 1999a). Further testing of the AMF wavelength choice was done using simulated Level 1 GOME/ERS-2 radiances in Van Roozendael et al., (2002), and it was shown that with this choice of 325.0 nm, total ozone errors of up to 5% are possible for solar zenith angles in excess of 80°, and generally, errors at the 0.5-1% level are found for sun angles < 80°. In the same study, it was shown that these errors are reduced (to the 1-2% level for SZA> 80°) when 325.5 nm is used as the representative AMF wavelength. The impact of the change in wavelength for the computation of the ozone AMFs is illustrated in Fig. 4. The ozone vertical column error displayed in Fig. 4 (lower panel) includes all basic aspects of the DOAS retrieval approach (except for cloud effects), and can be regarded as the "best-case "accuracy that can be expected from actual GOME and GOME-2 retrievals. The analyses of Spurr et al. (2010) show that errors below 2% are obtained for SZA < 87º in all typical GOME-2 observation conditions.

LIDORT is pure scattering code, and requires as input the following optical properties in each layer: (1) total extinction optical thickness, (2) total single scatter albedo, and (3) total phase function scattering coefficients. LIDORT also requires knowledge of the surface reflection (assumed Lambertian). In the GDP, there is an "atmospheric/surface setup module" which deals with detailed radiative transfer physics of molecules, trace gases, aerosols, clouds and surface reflection as needed to create the necessary LIDORT inputs. This setup function is completely decoupled from LIDORT, and this gives the AMF computation great flexibility. It is straightforward to change input climatology and other reference atmospheric and surface datasets. The setup function is described in the next section.

2.3.5 Atmospheric and surface setups for the RT model

As noted above, GDP 4.8 uses pressure levels from the TV8 ozone profile climatology. Top of the atmosphere (TOA) is set at 0.03 hPa. Temperature profiles are required for hydrostatic balance and the determination of ozone cross sections. A zonal mean (18 latitude bands) and monthly mean temperature climatology is supplied with the TV8 ozone profiles. Altitudes are determined by hydrostatic balance, with the acceleration due to gravity varying with latitude and height according to the specification in Bodhaine et al. (1999). For surface topography, the GDP uses the GTOP30 topographical database (http://lpdaac.usgs.gov/gtopo30/gtopo30.asp). In the calculation of ozone absorption optical thickness, the O_3 cross sections (as used in the DOAS fitting) are interpolated quadratically to account for the temperature dependence.
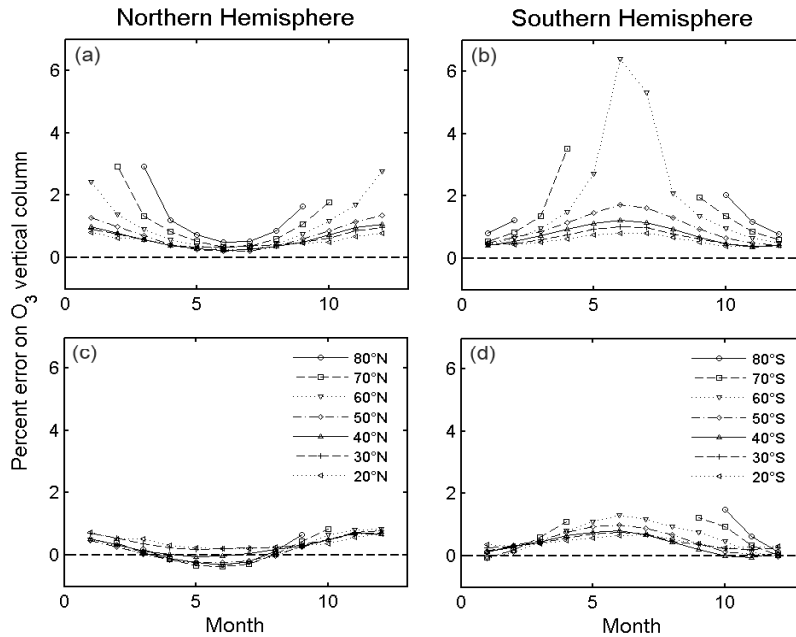
Figure 4   Impact on the total ozone accuracy of the choice of single wavelength for ozone AMF computations. Retrievals were made using synthetic radiance data based on the ozone profile climatology of Fortuin and Kelder (1998) (12 months, 7 latitude bands, both hemispheres). Panels (a) and (b): percentage error on total ozone columns for AMFs calculated at 325.0 nm. Panels (c) and (d): percentage error on total ozone with AMFs at 325.5 nm (from Van Roozendael et al. (2006)).

Rayleigh scattering is determined from a standard formula, but using the latest parameterizations as given in Bodhaine et al. (1999). The Rayleigh phase function depolarization ratio is taken from Chance and Spurr (1997). In GDP 4.8 total ozone retrievals, aerosols are neglected in the AMF computations, since AMF and VCD values are insensitive to aerosols to first order. For sensitivity testing, we have used the MODTRAN aerosol data sets (Kneizys et al., 1988) to provide aerosol loading and optical properties. We return to the aerosol sensitivity issue in Sect. 2.6 below.

In the GDP, a dynamic albedo data set derived from accumulated satellite reflectance data is used: a combination of the GOME Lambertian equivalent reflectivity (LER) data set of albedos prepared from 5.5 years of reflectivity data (Koelemeijer et al., 2003), and the Nimbus-7 TOMS LER data set prepared from 14.5 years of data from 1978 (Herman and Celarier, 1997), and valid for 340 and 380 nm. The GOME LER data has monthly and yearly entries on a 1°x1° latitude/longitude grid, at 12 different wavelengths spanning the GOME range; the TOMS data is also monthly. We use GOME LER data at 335 and 380 nm, and TOMS LER data at 380 nm; the desired combination albedo is $a(\lambda) = s(\lambda)a_{TOMS}(380)$, where the scaling is $s(\lambda) = a_{GOME}(\lambda)/a_{GOME}(380)$, and λ = 335 nm for total ozone fitting (Boersma et al., 2004). In this way, the strengths of both data sets are combined: the long duration of the TOMS record (1978-1992) and the spectral information (11 wavelengths) of the shorter GOME record (1995-2001).

Changes in surface albedo values will chiefly affect the clear-sky AMF M_{clear} and the intensity-weighted cloud fraction w. The effect on the total ozone column is largest for cloud-free and partly cloudy scenes; for completely cloud-covered scenes the effect is generally small, since the clear-sky AMF plays no part in the total ozone column calculations (see Eq. (3) with w = 1).

In the independent pixel approximation, cloud information is reduced to the specification of 3 parameters (cloud fraction, cloud-top albedo and cloud-top pressure). Clouds are regarded as highly reflecting Lambertian surfaces. GDP 4.8 employs the OCRA and ROCINN cloud pre-processing steps before the total column retrieval. OCRA uses the GOME-2 sub-pixel PMD output and it delivers the radiometric cloud fraction (Loyola, 1998). ROCINN (Loyola, 2004) is a fitting algorithm using O_2 A band reflectivities from GOME-2, and it retrieves cloud-top pressure and cloud-top albedo. Cloud fraction in the ROCINN algorithm is constrained to take the OCRA value when the algorithms are used in tandem. The algorithms are summarized in Chapter 0. The GDP, can ingest cloud results derived from other algorithms, e.g. the FRESCO cloud parameters provided in the GOME-2 Level 1b data.

2.4 Molecular Ring correction

The smoothing ("filling-in") of Fraunhofer features in zenith sky spectra was reported in Grainger and Ring (1962) and has become known as the Ring effect. It is also present in satellite instruments measuring in the UV and visible. It is now known to be caused in large part by inelastic rotational Raman scattering (RRS) from air molecules. The Ring reference spectrum is defined as the change in optical depth between intensities calculated with and without RRS. The Ring effect is generally small, as RRS contributes only 4% of all scattering by air molecules. The Ring effect shows up best in spectral regions of significant intensity modulation such as the well known Fraunhofer Ca II lines around 394-398 nm. However, modulations of backscattered light in the ozone Huggins bands are also large enough for inelastic RRS effects to appear as the filling-in of ozone absorption features (the molecular or telluric Ring effect). Spectral dependence in this molecular Ring effect correlates quite strongly with the behavior of the ozone absorption.

As noted in Sect. 2.2, the Ring effect is treated as "pseudo-absorber" interference in the DOAS algorithm using a Ring reference spectrum and additive fitting parameter. It was found that neglect of the telluric Ring effect for GOME in GDP 3.0 leads to systematic underestimation of ozone total columns (up to 10%) (Van Roozendael et al., 2002). From this study, a correction for the molecular Ring effect in ozone retrieval was developed during the GOME geophysical validation campaign in 2002, as explained below.

Considering only O_3 absorption, the correction is based on a simplified forward model of the intensity at satellite $I(\lambda)$ which includes an explicit contribution due to inelastic RRS:

$$I(\lambda) = I_0(\lambda) \cdot \exp\left[-\sigma_{O3}(\lambda) \cdot S_{O3} - P_1^\lambda\right] + E_{Ring} \cdot I_0^{RRS}(\lambda) \cdot \exp\left[-\sigma_{O3}(\lambda) \cdot S_{O3}^{out} - P_2^\lambda\right]. \qquad (8)$$

The first term on the right-hand follows the Lambert-Beer law for ozone absorption, with $I_0(\lambda)$ the solar intensity, and σ_{O3} and S_{O3} the ozone absorption cross-section and effective slant column respectively. Elastic scattering effects are subsumed by means of the low band pass polynomial P_1^λ. The Ring effect is modeled by the second term in Eq. (8), in which there are several approximations. First, it is assumed that Raman-scattered light is generated close to the surface of the atmosphere, with the spectral shape given by a source spectrum for Raman scattering $I_0^{RRS}(\lambda)$. This source spectrum only treats the spectral smoothing effect of RRS on the solar intensity. In practice it is calculated by the convolution of a GOME/GOME-2 irradiance spectrum using Raman cross sections appropriate to inelastic scattering into the wavelength of interest. The fractional intensity of Raman light (represented by the E_{Ring} parameter) may vary considerably depending on parameters such as cloud coverage, cloud altitude and surface albedo. Ozone absorption in the outgoing light path (the term $\sigma_{O3}(\lambda).S_{O3}^{out}$) is treated assuming that Raman photons produced at the surface and/or above clouds travel upward to the satellite. Ozone absorption taking place in the incoming light path is assumed to be fully smeared out in the inelastic process, so that it can be neglected in good approximation (error on total ozone <<1%).

Raman scattered light smoothes out structured information in incident solar radiation. It can be seen as a source of atmospheric stray light which produces a low-side bias on any retrieved trace gas total

column. This bias will nevertheless be modulated by atmospheric absorption in light paths above the region of RRS generation in the lower troposphere. For ozone, the bulk of the column is located in the stratosphere and upper troposphere, mostly above the source of RRS. Hence, ozone absorption that takes place in RRS light can be easily estimated. This is not necessarily the case for other trace gases, which may have significant partial columns in the lower troposphere. In summary, Raman scattering has a similar impact on all atmospheric absorbers, but it can only be accounted for accurately in a simple way for stratospheric trace gases such as O_3.

2.4.1 DOAS implementation

After two steps of linearization justified by the optically thin regime, Eq. (8) can be rewritten in the following way:

$$\ln\left[\frac{I(\lambda)}{I^0(\lambda)}\right] = -\sigma_{O3}(\lambda) \cdot S'_{O3} + \sigma_{Ring}(\lambda) \cdot E_{Ring} - P(\lambda),\tag{9}$$

with the Ring cross-section $\sigma_{Ring}(\lambda)$ defined as:

$$\sigma_{Ring}(\lambda) = \frac{I_0^{RRS}(\lambda)}{I^0(\lambda)}.\tag{10}$$

Equation (9) is the familiar DOAS fitting model, from which $S'_{O3,}$ E_{Ring} and the $P(\lambda)$ polynomial coefficients can be derived in the usual manner. The major difference with Ring correction methods used in previous studies comes in the definition of the modified ozone effective slant column $S'_{O3,}$ which is related to the effective slant column for *elastic* scattering (S_{O3}) by the following formula:

$$S'_{O3} = S_{O3} \cdot \left\{ 1 - E_{Ring} \cdot \overline{\sigma}_{Ring} \cdot \left(1 - \frac{\sec(\theta_0)}{M_{total}}\right) \right\} = S_{O3}.C_{Ring},\tag{11}$$

where M_{total} is the ozone AMF and θ_0 the viewing zenith angle. $\overline{\sigma}_{Ring}$ represents a mean Ring cross-section calculated over the spectral fitting interval. Doing this, we neglect the spectral modulation introduced by $\sigma_{Ring}(\lambda)$ since this effect is small in amplitude (a few percent). Although this approximation probably adds to the variance of the DOAS fit residuals, it greatly simplifies the correction scheme without compromising significantly the accuracy.

Equation (11) defines the molecular Ring correction C_{Ring}. From Sect. 2.3, we have $M_{total} = (1-w) \cdot M_{clear} + w \cdot M_{cloud}$ in the independent pixel approximation, where w is the intensity-weighted fractional cloud cover. In this formulation, the DOAS fitting is essentially unchanged, and it gives fitted parameters S'_{O3} and E_{Ring}. The effective slant column for ozone is then adjusted *after* the fit through the relation $S_{O3} = S'_{O3} / C_{Ring}$. Note that the molecular Ring term C_{Ring} can also be used to quantify the error due to an incorrect estimation of the Ring effect in older GDP versions. For the calculation of M_{total} in Eq. (11), we use the LIDORT-calculated total AMF already computed at each AMF/VCD iteration step to obtain C_{Ring} and the corrected slant column $S_{O3} = S'_{O3} / M_{Ring}$ as required for the VCD update (Eq.(6)).

Figure 5 shows values of the molecular Ring correction term C_{Ring} for four seasonally representative GOME-2/MetOp-A orbits. The ozone slant columns are scaled up by 2 to 9%. The general shape of the correction factor is due to the variation of SZA across the GOME-2 orbit. Pronounced peaks and high-frequency oscillations are mainly due to clouds, but changes of surface albedo and surface height can influence the correction. The cloud impact is especially visible for orbit 6429 (black) at latitudes of 10° N and 10° S where the GOME-2 measurements were affected by high clouds and the high cloud

fractional cover typically found in tropical regions. With RRS dominant in the lower troposphere, high cloud cover implies an immediately noticeable reduction in the RRS contribution to the measured radiance, and a consequent reduction in the Ring correction factor (closer to unity).
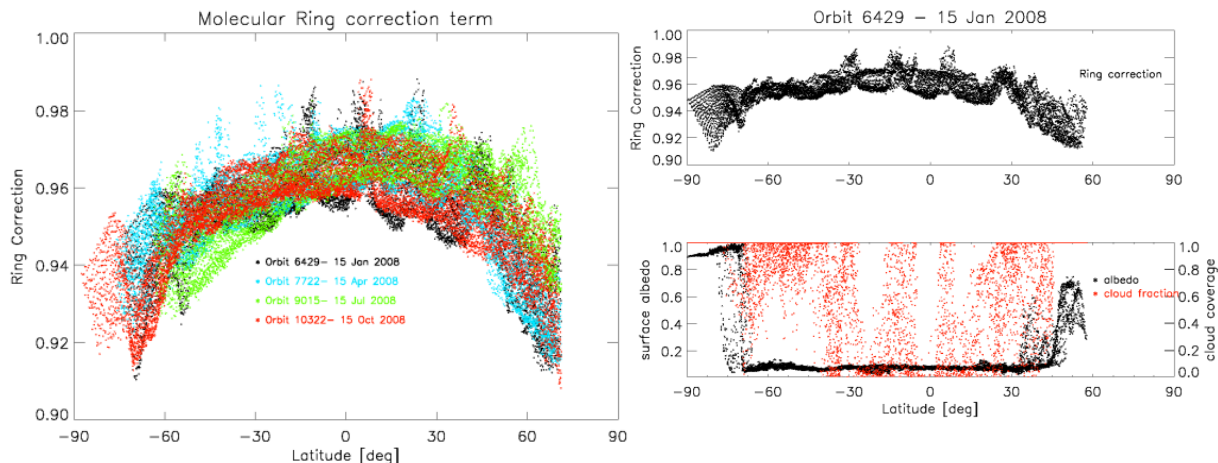

Figure 5   Molecular Ring correction factors (C_{Ring}) for four GOME-2/MetOp-A orbits in 2008 (left panel) and Ring correction, surface albedo and fractional cloud cover for one GOME-2 orbit (right panel).

2.5 Empirical correction for biases in GOME-2 total ozone

The GOME-2 vertical ozone columns show systematic biases of about 1.5% - 2% in both the latitudinal and scan directions. Systematic biases observed in the GOME-2 ozone retrievals with latitudinal dependency are likely due to changes in the slit-function over the orbit (because of on-board optical bench temperature changes). However, deficiencies in the key-data and the limited knowledge of the U-Stokes fraction could play a role as well. Deficiencies in the treatment of polarisation in the radiative transfer modelling can result in biases in both the latitudinal and scan direction. Finally, possible issues with the scan-angle dependent instrument key-data can result in a scan angle dependency of the GOME-2 ozone columns as well.

In the GDP 4.8, we use an empirical correction for the scan angle dependency which removed almost completely this dependency in the 24 forward scans from GOME-2. Scan angle read-outs toward the middle ground pixels were selected as reference for the correction (Hao et al., 2014). Seven years of GOME-2/MetOp-A data and two years of GOME-2/MetOp-B data are used to calculate these correction factors which are the function of scan angle, latitude and month. Figure 6 shows the empirical correction factors for GOME-2/MetOp-A for the months of January and July. Outside of the valid latitudinal range we reduced the correction factor to 1 (i.e. no correction) by interpolating between the last valid value and 1 for ±90º latitude. Look-up table of polynomial fitting parameters with the scan angle correction dependent on month, latitude and scan angle has been integrated into the GDP 4.8.
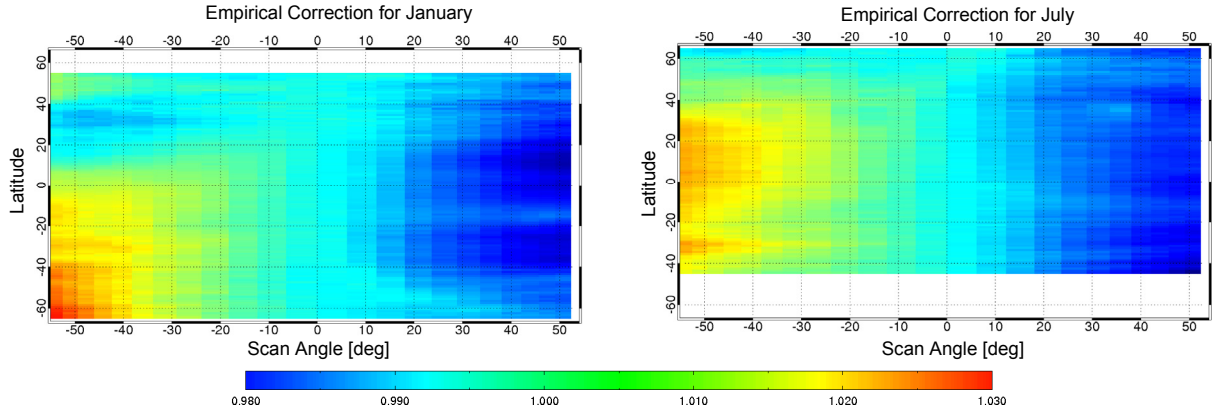
	REFERENCE:	**SAF/AC/DLR/ATBD/01**
	ISSUE:	3/A | Rev. 2
	DATE:	27.06.2017
	PAGE:	26

EUMETSAT AC SAF
ATMOSPHERIC COMPOSITION MONITORING

Figure 6 Empirical correction factors for the scan angle dependency for GOME-2/MetOp-A as function of latitude and scan angle (-50°=East;+50°=West) for January and July. Correction ratios larger than one (red) correspond to the Eastern part of the scan, while correction factors smaller than one (blue) correspond to the Western part of the scan.

2.6 Error budgets and sensitivity studies

2.6.1   Error budgets for the total ozone algorithm

Referring to Eq. (3) in Sect. 2.3, the error on vertical column V (denoted as s_V) can be expressed as a function of the error on component parameters S (ozone slant column), G (ghost vertical column), w (radiance-weighted cloud fraction), M_{clear} (AMF for a clear sky scene), M_{cloud} (AMF to cloud-top). A complete definition can be derived from error propagation rule:

$$s_V^2 = \left(\frac{\partial V}{\partial S}\right)^2 \cdot s_S^2 + \left(\frac{\partial V}{\partial M_{clear}}\right)^2 \cdot s_{M_{clear}}^2 + \left(\frac{\partial V}{\partial M_{cloud}}\right)^2 \cdot s_{M_{cloud}}^2 + \left(\frac{\partial V}{\partial w}\right)^2 \cdot s_w^2 + \left(\frac{\partial V}{\partial G}\right)^2 \cdot s_G^2. \qquad (12)$$

This error propagation formula is strictly valid under the assumption that error sources are mutually uncorrelated. In general we would expect some correlations (for example between the cloud fraction, and cloud-top height and cloud-top albedo), but the derivation of a complete error covariance for all sources is beyond the scope of the present work. With this in mind, we may use the definition of V in Eq. (3) to obtain:

$$\frac{\partial V}{\partial S} = \frac{1}{M_T}; \qquad \frac{\partial V}{\partial G} = w \cdot \frac{M_{cloud}}{M_T}; \qquad \frac{\partial V}{\partial w} = \frac{1}{M_T}\Big[V \cdot M_{clear} - (V - G) \cdot M_{cloud}\Big];$$

$$\frac{\partial V}{\partial M_{clear}} = -\frac{V}{M_T}(1-w); \qquad \frac{\partial V}{\partial M_{cloud}} = -\frac{V}{M_T}(1-w) \cdot$$

$$M_T = (1-w)M_{clear} + wM_{cloud}$$

Error component s_S comes from the DOAS slant column fitting, and s_w from the OCRA cloud pre-processing. An AMF error is assumed that is dependent on the solar zenith angle, and the ghost column error is taken as s_G = 30%. As discussed below, the solar zenith angle dependency of the AMF error has been determined empirically from an examination of the variability of the O_3 AMFs over a wide range of ozone profiles. It should be noted that this simplified error formulation is introduced for

the calculation of the errors on a pixel-by-pixel basis, and it only includes the largest contributors to the total error budget.

A more comprehensive estimation of the error budget for the GOME-2 ozone columns is provided in Table 3. This includes typical errors on ozone slant columns, ozone AMFs, cloud fractions and ozone ghost column, and are derived from the GDOAS delta-validation report for GOME/ERS-2 (Van Roozendael et al., 2004) and updated for the specific GOME-2 instrument characteristics (instrument signal-to-noise, viewing geometry etc.). The error budget has been separated into two parts: errors affecting the retrieval of slant columns (DOAS-related errors) and errors affecting the conversion of slant columns into vertical columns (AMF-related errors). Since several AMF-related error sources are significantly enhanced at large SZA, the AMF-related part of the error budget has been divided into two regimes (SZA < 80°, and SZA > 80°).

The DOAS-related (slant column) uncertainties are determined from a number of sensitivity tests dealing with the impact of uncertainties on absorption cross-sections and their temperature dependence, as well as wavelength calibration and convolution issues. We include the molecular Ring effect error under the DOAS heading. Errors due to the molecular Ring effect are derived from retrieval tests using synthetic radiance data, as presented in the GODFIT validation report (Van Roozendael et al., 2003). In addition, overestimation of ozone slant column (up to 5%) can occur in regions with large SO_2 abundance resulting from volcanic eruptions. Therefore, the ozone columns for GOME-2 pixels with large SO_2 column abundance (SO_2 column > 75 DU) are flagged in the GOME-2 L2 product.

Errors relating to O_3 AMF values are determined from a series of sensitivity tests carried out using different settings for the AMF calculations (e.g. different O_3 profile climatologies, or the error from the assumption of a single wavelength choice for the AMF calculation). In addition, the impacts of surface albedo errors as well as cloud and aerosol uncertainties have been considered explicitly. Several error sources are significantly enhanced at large solar zenith angles (typical of polar spring and autumn observations), and this justifies the division in the error budget in Table 3 between values representative of solar zenith angles lower than and greater than 80°. Independently of albedo and cloud/aerosol effects, errors on AMFs will depend significantly on the shape of the ozone profile as well as its column content. Hence an upper limit of the AMF error (and its SZA dependence) can be obtained from consideration of the variability of O_3 AMFs calculated using a wide range of climatological ozone profiles. The AMF variability is a strong function of the SZA, especially above 80°.

In an attempt to parameterize the main dependency of the AMF error, we have assumed that the AMF uncertainty can be linked to atmospheric profile shape errors, which will have a larger impact at high SZA values. For operational implementation in the GDP, this curve has been used to derive an empirical relationship between AMF uncertainty and solar zenith angle. A simple scaling (by a factor of 2) has been applied to the variability curve in such a way that the resulting error curve matches up with the error estimates shown in Table 3 for both SZA ranges. Although it is not the result of a rigorous error analysis, this empirical parameterization has the advantage of providing realistic uncertainties on the GOME-2 total ozone product both at low and at high SZA. The ghost column estimate of 30% used in GDP is a composite value based on error contributions from a number of sources (in particular, the ROCINN estimate of cloud-top height error and the uncertainty on the tropospheric part of the ozone profile).

2.6.2 Sensitivity issues for GDP 4.8 algorithm

The largest impact of atmospheric temperature is through the temperature-dependence of the ozone absorption cross-sections. Two ozone spectra at two different temperatures are used in the DOAS fitting; the accuracy of this approach is limited (1) at large SZA, due to the breakdown of the optically thin approximation, (2) at extreme stratospheric temperatures (due to non-linearity in the temperature dependence of the ozone cross-sections), and (3) by the intrinsic accuracy of the laboratory cross-sections. It is possible that instrument degradation also has an impact on the accuracy of the effective temperature determination. This has not been tested explicitly, but results from overpass processing over Hohenpeissenberg, extending from 2007 until 2013 and retrieved with no particular attempt to compensate for known GOME-2A degradation problems, suggest that the DOAS algorithm is stable and not strongly influenced by the degradation of the instrument (see Fig. 7).

Table 3 Estimation of error sources of the GOME-2 total ozone columns retrieved with the GDP 4.8 (partly based on Van Roozendael et al. (2004)].

Error source	Percent error	
	SZA < 80°	SZA > 80°
Ozone slant column		
O_3 absorption cross-sections	<2	<2
Atmospheric (effective) temperature determination	<1.5	<3
Instrument signal-to-noise	0.5 -1.0	<2
Instrument spectral stability (wavelength registration)	0.5	0.5
Solar I_0-effect	0.2	0.2
Ring and molecular Ring effect	<2	<2
Ozone Air Mass Factor		
Single wavelength calculation (325.5 nm)	<1	<2
O_3 profile	<1	<4
Surface albedo	0.3	0.3
Cloud fraction	0.8	0.8
Cloud top pressure (height)	1	1
Cloud top albedo (optical thickness)	0.8	0.8
Ghost column	<2	<3
Tropospheric aerosols (background conditions)	0.2	0.2
Ozone vertical column (accuracy)		
Clear	<3.6	<6.4
Cloudy	<4.3	<7.2
Ozone vertical column (precision)		
Clear	<2.4	<4.9
Cloudy	<3.3	<5.9

As noted already, the long-term stability of the GOME-2 total ozone record is a key consideration for trend analysis. In Fig. 7, monthly mean ozone differences between GDP 4.8 and Brewer measurements at Hohenpeissenberg are shown for a 6-year period from January 2007 through October 2013. This figure illustrates the long-term stability of GOME-2A and the absence of any significant time-dependent bias.

As described in Sect. 2.3, the GDP 4.8 uses the column-classified TOMS Version 8 ozone profile climatology for the AMF calculation. Since the iterative AMF/VCD algorithm relies on an ensemble of ozone profiles to define the profile-column map needed for the iteration, the choice of ozone profile climatology is important. Ozone profile shape is a key factor controlling the accuracy of the total ozone retrieval, especially at high latitudes where the ozone profile-shape sensitivity of the AMFs is enhanced by the extreme variations in the ozone field (e.g. ozone hole) combined with large solar zenith angles. The effect of using the two TOMS Version 7 and Version 8 ozone profile climatologies on the AMF and total ozone columns has been studied by Van Roozendael et al. (2006). Differences in retrieved GOME total ozone columns using the two climatologies are shown in Figure 8 for a sample data set consisting of 465 orbits from 1997. Largest differences are found in polar regions (especially in the southern hemisphere) close to the terminator where SZAs are at their maximum. In Spurr et al. (2005), it was noted that the fixed ozone burden in the troposphere was a significant error source for ozone AMFs in GDP 3.0, particularly at low SZA (maximum photon penetration). In the TV7 data set, ozone partial columns are fixed at 9 DU and 15 DU in the lowest two layers. There is much more tropospheric variation in ozone content with the Version 8 profile data, but it remains the case that

errors of 10-15 DU in the tropospheric boundary layer ozone burden can induce AMF errors of 3-5% for low SZA values (~25º). This may explain the surprisingly large sensitivity in Figure 8 for the Northern sub-tropics during summer when the SZA is at minimum.

It is difficult to extract any information about aerosols from a DOAS fitting of ozone in the UV Huggins bands. Aerosol scattering and extinction are subsumed in the DOAS slant column fit through the closure polynomial, and the introduction of parameterized aerosol information in the AMF RT simulations is an additional source of error. The policy in the GDP algorithms has been to avoid the use of aerosols altogether, and to use a Rayleigh atmosphere for the baseline AMF calculations. For scattering aerosols in the troposphere, the AMF is relatively insensitive to aerosol content. For background aerosol conditions the error is small: ~0.2%; for more optically thick aerosol regimes, the error generally remains below the 1% level. It is known however that for scenarios with absorbing aerosols present (in particular biomass burning, industrial pollution, desert dust outbreaks and volcanic plumes), ozone AMFs may be significantly in error if the aerosol presence is ignored or not treated accordingly. These effects are again largest for low SZA. This is because these aerosols are mostly concentrated in the lowermost layers of the atmosphere, and the sensitivity to these layers is largest at low SZAs. Aerosols are not treated explicitly in the GDP 4.8 AMF calculations. However, a significantly scattering aerosol layer will be detected by OCRA/ROCINN as a thin cloud layer, and the aerosol effect will thus be included indirectly in the vertical column calculation. To first-order, aerosol uncertainties in the total algorithm will be picked up in the cloud parameter error budget estimates. Although cloud fractions are in general weakly influenced by the presence of aerosols, cloud algorithms such as FRESCO and OCRA/ROCINN are sensitive to strong aerosol pollution episodes.
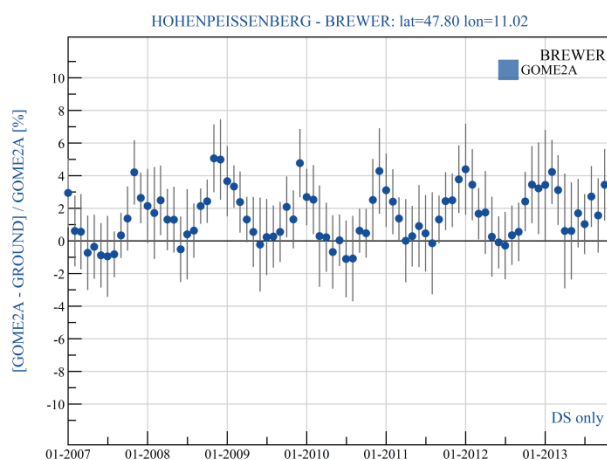

Figure 7 GOME-2/MetOP-A (GDP v4.8) – Hohenpeissenberg Brewer monthly mean ozone differences from January 2007 until October 2013.

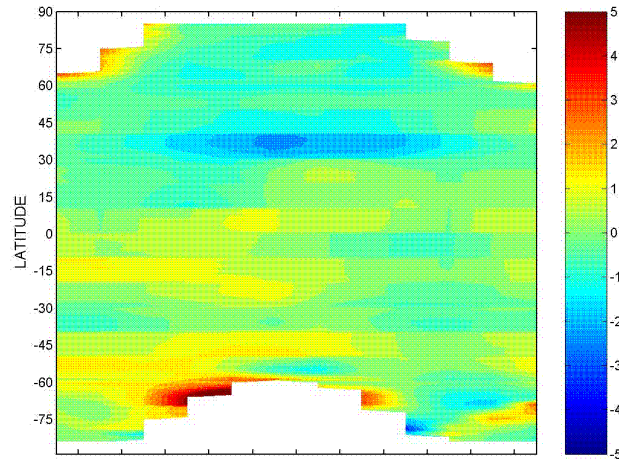|	REFERENCE:	**SAF/AC/DLR/ATBD/01**
	ISSUE:	3/A | Rev. 2
	DATE:	27.06.2017
	PAGE:	30

EUMETSAT
AC SAF
ATMOSPHERIC COMPOSITION MONITORING

Figure 8 Relative differences in GOME/ERS-2 total ozone retrieved using the two TOMS version 7 and version 8 ozone profile climatologies. Differences are mostly significant in polar regions, close to the terminator, as well as in northern tropical regions around the place of minimum solar zenith angle (from Van Roozendael et al. (2006)).

3   THE NO$_2$ COLUMN ALGORITHM

This chapter describes the retrieval of total and tropospheric NO$_2$ columns for GOME-2 (Valks et al., 2011). First, the NO$_2$ slant column retrieval using the DOAS method is described and in Sect. 3.2, the air mass factor and the total vertical column computation are discussed. Sect. 3.3 describes the tropospheric NO$_2$ column retrieval. An error assessment of the GOME-2 NO$_2$ columns is presented in Sect. 3.4.

3.1 DOAS slant column fitting

The GDP 4.8 NO$_2$ DOAS algorithm is similar to that for total ozone, and uses the same least squares fitting package; the description in Sect. 2.2 is relevant here, with the following specific NO$_2$ DOAS settings:

- The fitting window is 425-450 nm in GOME-2 Channel 3. NO$_2$ absorption features are prominent, and GOME-2 measurements have high signal-to-noise and manageable interference effects.
- A single NO$_2$ cross-section reference spectrum is used. In the GDP 4.8, the Vandaele et al. (2002) cross-section at 240 K is used (convolved with the GOME-2 FM3/FM2 slit functions (Siddans et al., 2006, 2012)).
- Ozone is an interfering species and is included in the DOAS fit. However, ozone absorption in this part of the Chappuis bands is weak (one reason for the fitting window choice). In this wavelength region, the GOME-2 FM3 and FM2 cross-sections data at 221 K can be used (Gür et al., 2005).
- O$_2$-O$_2$ and H$_2$O are interfering species and slant column amplitudes for them are included in the fit. Sources are Greenblatt et al. (1990) for O$_2$-O$_2$ (recalibrated) and HITRAN (Rothman et al., 2003) for H$_2$O (the latter as input to line-by-line computations which are followed by GOME-2 FM3/FM2 slit function convolution).
- One additive Fraunhofer Ring spectrum is used for the DOAS retrieval in the VIS wavelength range in GOME-2 Channel 3 (similar as for the total ozone retrieval).
- There is no molecular Ring correction implemented for the NO$_2$ retrieval. The error in the retrieved total column due to the molecular Ring effect is small (1-2%) as compared to the other error sources (see also Sect. 3.4).
- Intensity offset effects that may be induced by residual stray-light or remaining calibration issues in the level-1 product are known to be sources of bias in DOAS retrievals of minor trace species. To correct for this, a linear offset correction is used by including an inversed Earth-shine spectrum as additional effective cross-section in the DOAS fit
- The broadband filtering polynomial is cubic (4 coefficients).

The total number of fitting parameters is 10, comprising 4 trace gas slant columns, 4 polynomial coefficients, and 2 amplitudes for additive reference spectra. Wavelength registration is done as for total ozone DOAS: the solar spectrum is the wavelength standard, with a shift-and-squeeze fitting performed for each footprint for resampling the earthshine spectrum. "Post Level 1" wavelength registration for the solar spectrum is improved at the orbit start by an additional cross-correlation covering the 425-450 nm fitting window.

The NO$_2$ absorption cross-section has a marked temperature dependence, which has to be taken into account to improve the accuracy of the retrieved columns. In the GDP, a single NO$_2$ cross-section reference spectrum at 240 K is used, and an a posteriori correction for the difference between the atmospheric temperature and the 240 K cross-sections temperature is performed on the air mass factor level (see Sect. 3.2)

3.2 AMF and initial total VCD computation

The second component in the retrieval is the conversion of the NO$_2$ slant column density S into the initial total VCD V_{init}, using the air mass factor M:

$$V_{init} = \frac{S}{M} \tag{13}$$

The air mass factor depends on the vertical NO_2 profile and a set of forward model parameters **b**, including the GOME-2 viewing geometry, surface albedo, clouds and aerosols. For optically thin absorbers, such as NO_2 in the visible wavelength region, the radiative transfer calculations can be decoupled from the trace gas profile shape:

$$M = \frac{\sum_l m_l(\mathbf{b}) x_l c_l}{\sum_l x_l} \tag{14}$$

where m_l is the air mass factors for the individual layer l (independent of the NO_2 profile), and x_l the partial NO_2 column in layer l. The altitude-dependent air mass factors m_l are calculated with the LIDORT radiative transfer model for the window mid-point (437.5 nm), since NO_2 is an optically thin absorber in this wavelength region. The coefficients c_l are layer-specific correction factors that account for the temperature dependence of the NO_2 absorption cross-section. This correction factor is a function of the atmospheric temperature in layer l and the fixed temperature (240K) of the NO_2 absorption cross-sections assumed in the DOAS fit (Boersma et al., 2004). In the GDP, monthly mean temperatures taken from a run of the MOZART-2 model (see next section) are used to calculate the correction factors for the tropospheric layers.

The initial total VCD is computed under the assumption that the troposphere is not polluted. Therefore, the air mass factor is based on stratospheric NO_2 profiles only, whereas the tropospheric NO_2 amount is assumed to be negligible. This approach is valid over large parts of the Earth, but in areas with significant tropospheric NO_2, the total column densities are underestimated and need to be corrected, as described in the next section. To incorporate the seasonal and latitudinal variation in stratospheric NO_2 in the air mass factor calculations, a harmonic climatology of stratospheric NO_2 profiles is used (Lambert and Granville, 2004). The climatology used for the surface albedo (including mean snow and ice cover) is derived from TOMS and GOME Lambert-equivalent reflectivity (LER) measurements at 380 and 440 nm, as described in Boersma et al. (2004).

For GOME-2 scenarios in the presence of clouds, the air mass factor can be determined in conjunction with GOME-2 derived cloud information (see Chap. 0) using a Lambertian reflecting boundary cloud model and the independent pixel approximation (IPA):

$$M = (1-w)M_{clear} + wM_{cloud}, \tag{15}$$

where M_{clear} is the air mass factor for a completely cloud free pixel, M_{cloud} the air mass factor for a completely cloudy pixel, and w the cloud radiance fraction. M_{clear} and M_{cloud} are obtained with Eq. (14), with clouds treated as Lambertian equivalent reflectors and M_{cloud} calculated with $m_l = 0$ for all layers below the cloud-top pressure. The intensity weighted cloud fraction (or cloud radiance fraction) w is defined in Eq. (4).

3.3 Tropospheric NO_2 column calculation for polluted conditions

The tropospheric NO_2 column algorithm for GOME-2 consists of the following steps: 1) calculation of the initial total NO_2 column as described above, 2) estimation of the stratospheric component of the NO_2 column using a spatial filtering approach and 3) the conversion of the residual tropospheric slant column into a tropospheric vertical column, using an accurate tropospheric air mass factor (including the effects of clouds). In addition, the initial total NO_2 column is corrected for the tropospheric component under polluted conditions, to provide a more accurate total vertical column. A description of these algorithm steps is given below.

3.3.1 Stratospheric correction

After the calculation of the initial total NO_2 column, the next step in the retrieval of the tropospheric NO_2 column is the estimation of the stratospheric component from the initial total VCD. The stratosphere-troposphere separation (STS) is based on the observation that stratospheric NO_2 has a smooth spatial behaviour and that tropospheric contributions occur near source regions on smaller geographic scales. The STS algorithm employed for GOME-2 in the GDP uses a spatial filtering method: First a global map is constructed from the initial NO2 columns by binning the last 24 hours of GOME-2 data on a spatial grid of 2.5º latitude × 2.5º longitude. To minimize tropospheric biases in the stratospheric field, a global mask is applied to eliminate areas with potentially high amounts of tropospheric NO_2. This pollution mask is derived from MOZART-2 model results: the areas in the model with monthly mean tropospheric NO_2 columns larger than $1.0×10^{15}$ molec/cm^2 are masked as polluted (see next section).

After pollution masking, the stratospheric NO_2 column is determined by low-pass filtering the initial NO_2 columns in the zonal direction (30º boxcar filter). This is done in two steps, where first the unmasked measurements with initial total VCD exceeding the (preliminary) stratospheric NO_2 column by more than one standard deviation are identified and excluded from the final analysis. Unmasked polluted measurements can occur when pollution events are missed by the model, for instance during transient pollution events. Finally, the stratospheric NO_2 is interpolated between latitude bands in order to avoid jump artefacts associated with a discrete latitude grid.

A limitation of the spatial filtering approach used here is that it will also take up background NO_2 in the free troposphere with smooth spatial behaviour. In the GDP, a simple correction is applied for this effect: a fixed background NO_2 column ($0.1×10^{15}$ molec/cm^2) is subtracted from the derived vertical stratospheric NO_2 column. This offset for the background NO_2 column has been derived from tropospheric NO_2 fields for the (unpolluted) Pacific region, as provided by the MOZART-2 model.

An example of the stratospheric NO_2 distribution obtained with the spatial filtering approach used in the GDP is plotted in Figure 9. This figure shows the initial total and stratospheric NO_2 columns from GOME-2 for the northern mid- and high-latitudes on 22 February 2008. Clearly visible in this figure are the longitudinal variations in stratospheric NO_2. The low values over the north polar area around Greenland and Eastern Canada indicate denoxified air masses inside the polar vortex. Due to dynamical variability, the location of these air masses can vary strongly within a time scale of a few days. Figure 9 shows that a large part of the area over the northern Atlantic with low NO_2 is captured by the spatial filtering approach on this day (which would not have been possible with the Pacific Reference Sector method). However, the stratospheric NO_2 column over parts of Northwestern Europe is overestimated by the stratospheric correction procedure, which results in an underestimation of the tropospheric NO_2 column.

3.3.2 Tropospheric Air Mass Factor and VCD computation

After the stratosphere-troposphere separation, the tropospheric VCD can be determined via the relation:

$$V_t = \frac{S - M_s V_s}{M_t} \tag{16}$$

where S is the slant column density calculated in the DOAS fit and V_s is the stratospheric component, as calculated with the spatial filtering method described above. M_s is the stratospheric air mass factor, used for the calculation of the initial total VCD, as described in Sect. 3.2. M_t is a tropospheric air mass factor calculated with Eq. (14) and Eq. (15), using an a priori tropospheric NO_2 profile. The tropospheric air mass factor depends on the same forward model parameters as the stratospheric air mass factor (i.e. GOME-2 viewing geometry, surface albedo, clouds and aerosols). However, the

dependence on the surface albedo, clouds and aerosols, as well as the a priori NO_2 profile is much stronger for the tropospheric air mass factor.
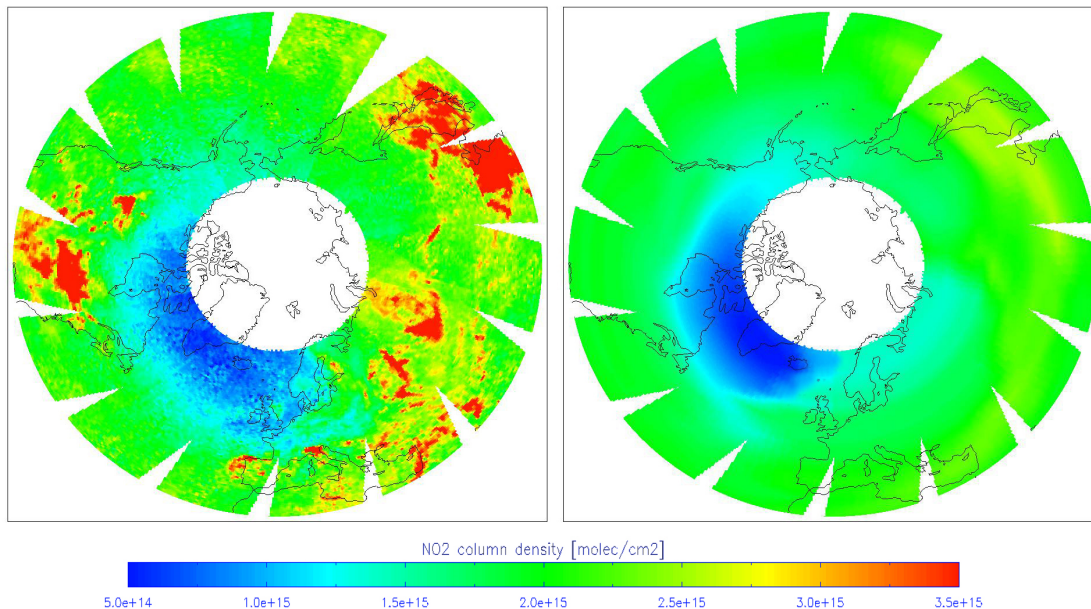

Figure 9 Total NO_2 distribution from GOME-2/MetOp-A for 22 February 2008 (left) and the corresponding stratospheric NO_2 distribution as obtained with the spatial filtering approach (right).

After the calculation of the tropospheric column, a corrected total VCD V_c can be calculated via the relation:

$$V_c = V_s + V_t \tag{17}$$

In the GDP, the tropospheric VCD and a corrected total VCD are determined for all GOME-2 observations where the initial total VCD exceeds the estimated stratospheric component V_s. In these cases, the stratospheric component V_s, the tropospheric column density V_t and corrected total vertical column density V_c are provided in the GOME-2 L2 data product, as well as the initial vertical column density V_{init}.

The a priori NO_2 profiles are obtained from a run of the global chemistry transport model (CTM) MOZART version 2 (Horowitz et al., 2003). The model data has a horizontal resolution of 1.875° latitude by 1.875° longitude (T63), with 32 terrain-following hybrid layers extending from the surface up to ~3 hPa. The number of layers in the troposphere varies from 10 to 16, depending on tropopause height, with about 4 layers in the boundary layer. For the tropospheric air mass factor computation in the GDP, monthly average profiles at the satellite overpass time have been determined (Nüß et al., 2006). While this climatology will capture seasonal and spatial patterns and provides a good first guess of the atmospheric NO_2 profile, daily data from an online model run can capture short-term variability induced by meteorology and would therefore be preferable (Boersma et al., 2004). This option is currently under consideration for future versions of the GDP.

The calculation of the tropospheric VCD is complicated in case of (partly) cloudy conditions. For many measurements over cloudy scenes, the cloud-top is well above the NO_2 pollution in the boundary layer, and when the clouds are optical thick, the enhanced tropospheric NO_2 concentrations cannot be detected by GOME-2. Therefore, the tropospheric VCD calculated for observations with a cloud radiance fraction $w > 50\%$ are flagged in the GOME-2 L2 product. Note that the "below cloud amount" (i.e. the amount of NO_2 that is inferred to be below the cloud top) for these partly cloudy conditions is implicitly accounted for via the cloudy air mass factor M_{cloud} (in which $m_l = 0$ for all layers below the

cloud-top). As this procedure assumes knowledge of the vertical NO_2 profile (taken from the model) and neglects any possible differences of this profile in the cloudy and cloud-free part, cloudy scenes will have higher uncertainty than clear sky observations.

The tropospheric air mass factor M_t and the altitude-dependent air mass factors m_l are used to compute the so-called DOAS-type averaging kernels A_l (Eskes and Boersma, 2003):

$$A_l = \frac{m_l}{M_t} \qquad (18)$$

Column averaging kernels are essential information on the measurement vertical sensitivity and are particularly useful when comparing measured columns with e.g. model simulations, because they allow removing the effect of the a priori profile shape information used in the retrieval and is required for comparison with other types of data. The DOAS averaging kernels for the retrieved tropospheric NO_2 columns are included in the GOME-2 level-2 product.

3.4 Error budget for the total and tropospheric NO_2 column

An estimation of the error budget for the GOME-2 total and tropospheric NO_2 column is provided in Table 4. This includes typical errors on NO_2 slant columns and the AMF for the total NO_2 column for unpolluted conditions, and the tropospheric NO_2 column (for polluted conditions). The error-estimates are mainly based on initial DOAS analyses using GOME-2 data (see Section B in Lambert et al. (2007)), and the NO_2 error analysis of Boersma et al. (2004) and Valks et al. (2011). A detailed error analysis and description of the different error sources in the GOME-2 NO_2 product can be found in Valks et al. (2011).

Table 4 Estimation of error sources for the total NO_2 column for unpolluted conditions and the tropospheric NO_2 column (for polluted conditions) retrieved with the GDP 4.8. See Valks et al. (2011) for a detailed error analysis and description of the different error sources in the GOME-2 NO_2 product.

Error source	Percent error	
	Total column (unpolluted)	**Tropospheric column (polluted)**
NO_2 slant column		
NO_2 absorption cross-sections	2-5	2-5
Instrument signal-to-noise	5	5
Instrument spectral stability (wavelength registration)	0.5	0.5
Ring and molecular Ring effect	<2	<2
Stratospheric NO_2 column	n.a.	10-20
NO_2 Air Mass Factor	2-5	15-50
NO_2 vertical column (accuracy)	5-15	40-80

4   THE BRO COLUMN ALGORITHM

4.1 DOAS slant column fitting

The DOAS algorithm for BrO is based on the DOAS algorithm for ozone as described in detail in Sect. 2.2. The original GOME algorithm used the 344.7-359 nm wavelength range for the DOAS slant column fit of BrO (so-called "GOME" fitting-window) (Richter et al., 1998). As a result of the smaller pixel size of GOME-2 observations (40x80 / 40x40 km^2 instead of 40x320 km^2 for GOME), the noise on the individual GOME-2 BrO measurements was found to be significantly increased in comparison to GOME. Therefore, an alternative UV shifted fitting window of 336–351.5 nm that has already been used for SCIAMACHY measurements (so-called "SCIAMACHY" fitting-window) was introduced in the GDP 4.3, which significantly reduced the noise level compared to the "GOME" fitting window. In the GDP 4.5, improved BrO DOAS settings have been implemented with the objective to stabilize the fit as much as possible and to minimize interferences with other trace gases, especially formaldehyde (Theys et al., 2011). An important difference with respect to past settings relies in the choice of the fitting window which has been extended towards shorter wavelengths (332-359 nm) in order to cover five BrO absorption bands. The detailed DOAS settings for the GOME-2 BrO retrieval as used in the GDP 4.8 are listed below:

- The DOAS slant column fit is performed in a larger fitting window further extended towards shorter wavelengths to cover five BrO absorption bands (332-359 nm). In addition to a noise reduction, several unwanted artefacts could be minimized (viewing angle dependent slant columns, interference with formaldehyde absorptions over polluted areas, presence of cloud structures due to incomplete ring effect correction)
- A single BrO cross-section at 223K is included in the fit (Fleischmann et al., 2004).
- In addition, cross-sections of the interfering trace gases ozone at 228K and 243K (Brion et al., 1998), formaldehyde at 298K (Meller and Moortgat, 2000), OClO at 293K (Bogumil et al.,2003) and NO_2 at 220K (Vandaele et al., 2002) are included.
- The absorption cross-sections are convolved with the GOME-2 slit function (GOME-2A: Flight Model 3, GOME-2B: Flight Model 2) (Siddans et al., 2006, 2012).
- Compensation of the molecular ring effect is been realized by including two Ring reference spectra as additional fitting parameters calculated by the SCIATRAN model (Rozanov et al., 2001).
- To consider the strong ozone absorption in the extended fitting window below 336 nm, two additional fitting parameters are included in the DOAS analysis (Puķīte et al., 2010). Here, the O_3 slant columns as function of wavelength and optical depth are described by Taylor series. The Taylor coefficients provide two additional cross-sections for O_3 at 228K (original cross-section multiplied by wavelength and original cross-section squared).
- The broadband filtering polynomial is of 5th order (6 coefficients).
- To correct for intensity offset effects, that may be induced by residual stray-light or remaining level-1 calibration issues, a linear offset correction is used by including an inversed earth-shine spectrum as additional effective cross-section in the DOAS fit.
- Two additional polarization functions (Eta and Zeta from GOME-2 calibration key data) are included in the fit (EUMETSAT, 2011).

4.2   Equatorial offset correction

The instrumental degradation, strongly showing up during the advanced lifetime of GOME-2A, negatively influences DOAS fit residuals, the noise in the BrO columns, as well as the average slant columns values (see Figure 10). Therefore, an equatorial offset correction is applied on a daily basis to the BrO data (Richter et al., 2002). This correction enables to correct – to some extend – for the effect of the instrumental degradation on the total BrO column data time series.
For this correction, averaged BrO slant columns in the tropical latitudinal band between ±5° are calculated on a daily basis, assuming small equatorial BrO columns with no significant seasonal

variations. These averaged slant columns are then subtracted from all slant columns and a constant equatorial slant column offset of 7.5 x 10^{13} molec/cm² is added.
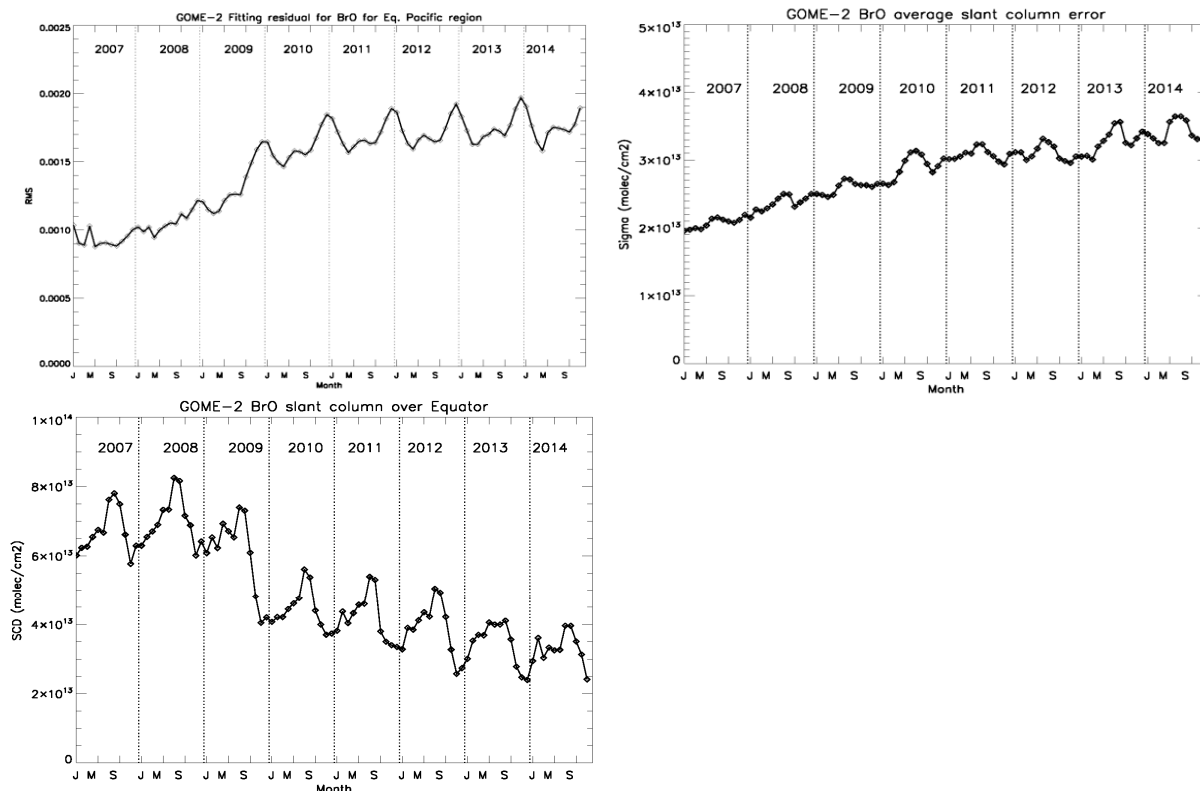

Figure 10   Long-term DOAS fitting residuals (top-left) and the (random) BrO slant column error (top-right) for the 332-359 nm BrO fitting window for GOME-2A. The monthly averaged residuals values and average slant column errors have been calculated for the equatorial Pacific region (10°S - 10°N, 160°E -160°W). The bottom figure shows the decrease in the average BrO slant column density (for the equatorial region) between 2007 and 2014 as a result of the GOME-2 instrument degradation.

4.3 AMF and VCD determination

The next step in the BrO column algorithm is the conversion of the slant column density *S* into the vertical column *V*, using the AMF *M*:

$$V = \frac{S}{M} \tag{19}$$

The AMF is calculated according to Eq. (2) using the LIDORT model for the fitting window mid-point (344 nm), since BrO is an optically thin absorber in this wavelength region. To incorporate seasonal and latitudinal variations in stratospheric BrO in the AMF calculations, a stratospheric BrO profile climatology is used (Bruns et al., 2003). This climatology contains monthly mean BrO profiles as a function of latitude, based on the chemistry transport model SLIMCAT.

For GOME-2 scenarios in the presence of clouds, the BrO air mass factor is determined using a Lambertian reflecting boundary cloud model and the independent pixel approximation (IPA):

$$M = (1-w)M_{clear} + wM_{cloud} , \tag{20}$$

where M_{clear} is the air mass factor for a completely cloud free pixel, M_{cloud} the air mass factor for a completely cloudy pixel, and w the cloud radiance fraction. No ghost column correction is applied for the BrO retrieval.

An error estimate for the GOME-2 total BrO columns is given in Table 5. Note that the retrieval of tropospheric BrO columns is planned at a later stage in the CDOP-2.

Table 5   Estimation of error sources for the total BrO column.

Error source	Percent error
BrO slant column	15-30
BrO absorption cross-sections	5-10
Instrument signal-to-noise	10-20
BrO Air Mass Factor	5-20
BrO vertical column (accuracy)	20-50

5   THE FORMALDEHYDE COLUMN ALGORITHM

5.1 DOAS slant column fitting

The DOAS algorithm for formaldehyde (HCHO) is based on the DOAS algorithm for ozone, as described in Sect. 2.2. To reduce the interference between HCHO and BrO absorption features, a two-step DOAS fit retrieval based on De Smedt et al. (2012) that effectively reduces the noise in the GOME-2 HCHO columns, has been implemented in the GDP 4.8. Firstly, BrO slant columns are fitted in the large wavelength range 332-359 nm that includes five BrO absorption bands and minimizes the correlation with HCHO. Then HCHO columns are retrieved in the wavelength range 328.5-346 nm, using the BrO slant column values determined in the first step. The detailed DOAS algorithm settings for HCHO are listed below.

First Step: DOAS slant column fit of BrO performed in the UV wavelength range 332-359 nm

- A single BrO cross-section at 223K is included in the fit (Fleischmann et al., 2004).
- In addition, cross-sections of the interfering trace gases ozone at 228K and 243K (Brion et al., 1998), HCHO at 298K (Meller and Moortgat, 2000), OClO at 293K (Bogumil et al.,2003) and NO_2 at 220K (Vandaele et al., 2002) are included.
- The absorption cross-sections are convolved with the GOME-2 slit function (Siddans et al., 2006, 2012).
- Compensation of the molecular ring effect is been realized by including two Ring reference spectra as additional fitting parameters calculated by the SCIATRAN model (Rozanov et al., 2001).
- To consider the strong ozone absorption below 336 nm, two additional fitting parameters are included in the DOAS analysis (Puķīte et al., 2010). Here, the O_3 slant columns as function of wavelength and optical depth are described by Taylor series. The Taylor coefficients provide two additional cross-sections for O_3 at 228K (original cross-section multiplied by wavelength and original cross-section squared).
- The broadband filtering polynomial is of 5th order (6 coefficients).
- To correct for intensity offset effects, that may be induced by residual stray-light or remaining level-1 calibration issues, a linear offset correction with an inversed earth-shine spectrum as additional effective cross-section is used.
- Two additional polarization functions (Eta and Zeta from GOME-2 calibration key data) are included in the fit (EUMETSAT, 2011).

Second Step: DOAS slant column fit of HCHO performed in the wavelength range 328.5-346 nm

- A single HCHO cross-section at 298K is included in the fit (Meller and Moortgat, 2000).
- In addition, cross-sections of the interfering trace trace gases ozone at 228K and 243K (Brion et al., 1998), OClO at 293K (Bogumil et al.,2003) and NO_2 at 220K (Vandaele et al., 2002) are included.
- BrO is not fitted: The BrO slant columns values determined in the first step are used.
- The absorption cross-sections are convolved with the GOME-2 slit function.
- The compensation of the molecular ring effect is been realized by including the same Ring reference spectra as additional fitting parameters as in the first step.
- To consider the strong ozone absorption below 336 nm, the same Taylor coefficients as additional cross-sections has been used as in the first step.
- The broadband filtering polynomial is of 5th order (6 coefficients).
- To correct for intensity offset effects, the same linear offset correction as in the first step is used.

Figure 11 illustrates the reduced scatter in the GOME-2 HCHO columns retrieved with the GDP 4.8 compared to the previous GDP version. This is mainly a result of the BrO slant column fit in a separate fitting window (332-359 nm).
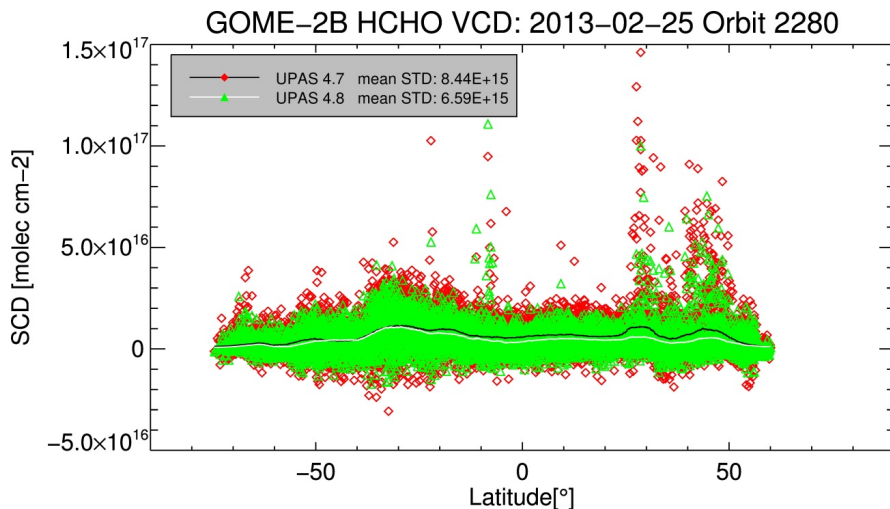
Figure 11   Single orbit of GOME-2B showing the reduced scatter in GDP 4.8 compared to GDP 4.7 due to implementation of a second fitting window for BrO. Plotted are the individual measurements and its averages (lines) within 5° latitude bands.

5.2 Reference sector correction

In the wavelength range 328.5 – 346 nm, there are still unresolved spectral interferences between the ozone and BrO absorption features resulting in obvious zonally and seasonally dependent artefacts. To reduce the impact of these artefacts, an absolute normalisation is applied on a daily basis using the reference sector method (Khokhar et al., 2005). The reference sector is chosen in the Pacific Ocean (Longitude: 140°-160° W), where the only source of HCHO is CH_4 oxidation. The mean HCHO slant column density in the reference sector is determined by a polynomial fit, which is then subtracted from the retrieved slant columns on this day ($\Delta S = S - S_0$), and replaced by a HCHO background value (V_0^{CTM}) taken from IMAGESv2 model results (see next section).

5.3 AMF and VCD determination

The AMF depends strongly on the vertical profile shape of HCHO in the troposphere, the surface albedo and the presence of clouds. Since HCHO is an optically thin absorber in this wavelength region, the air mass factor is calculated by decoupling the radiative transfer calculations from the trace gas profile shape (see Eq. (14)):

$$M = \frac{\sum_l m_l(\mathbf{b})x_l}{\sum_l x_l} \tag{21}$$

where m_l is the air mass factors for the individual layer l (independent of the HCHO profile), and x_l the partial HCHO column in layer l. The altitude-dependent air mass factors m_l are calculated with the LIDORT radiative transfer model for 335 nm.

The a priori HCHO profiles are obtained from a run of the tropospheric 3-D chemistry transport model (CTM) IMAGES version 2 (Mueller and Stavrakou, 2005). The model data has a horizontal resolution of 2.0° latitude by 2.5° longitude, with 40 vertical layers extending from the surface up to ~44 hPa. For the air mass factor computation in the GDP, monthly average HCHO profiles for the year 2007 are used. The surface albedo is obtained from the combined TOMS/GOME climatology (Boersma et al, 2004), see Sect. 2.3.

For GOME-2 scenarios in the presence of clouds, the air mass factor is determined using a Lambertian reflecting boundary cloud model and the independent pixel approximation (IPA):

$$M = (1-w)M_{clear} + wM_{cloud},$$ (22)

where M_{clear} is the air mass factor for a completely cloud free pixel, M_{cloud} the air mass factor for a completely cloudy pixel, and w the cloud radiance fraction. M_{clear} and M_{cloud} are obtained with Eq. (21), with clouds treated as Lambertian equivalent reflectors and M_{cloud} calculated with $m_l = 0$ for all layers below the cloud-top pressure. The cloud radiance fraction w is defined in Eq. (4).

The computation of the HCHO vertical column density V then proceeds via:

$$V = \frac{\Delta S}{M} + V_0^{CTM}$$ (23)

where ΔS is the differential slant column density of HCHO after the reference sector correction, and V_0^{CTM} the HCHO background value taken from the IMAGESv2 model, as described above. For many measurements over cloudy scenes, the cloud-top is well above the HCHO abundance in the boundary layer, and when the clouds are optical thick, the enhanced tropospheric HCHO concentrations cannot be detected by GOME-2. Therefore, the HCHO vertical columns retrieved for observations with a cloud fraction > 40% are flagged in the GOME-2 L2 product. Note that the "below cloud amount" (i.e. the amount of HCHO that is inferred to be below the cloud top) for these partly cloudy conditions is implicitly accounted for via the cloudy air mass factor M_{cloud} (in which $m_l = 0$ for all layers below the cloud-top). As this procedure assumes knowledge of the vertical HCHO profile (taken from the model) and neglects any possible differences of this profile in the cloudy and cloud-free part, cloudy scenes will have higher uncertainty than clear sky observations.

The DOAS averaging kernels A_l for the retrieved tropospheric HCHO columns are calculated using Eq. (18), in a similarly way as for the tropospheric NO_2 column (see Sect. 3.3.2). The GOME-2 level-2 product includes the DOAS averaging kernels for the retrieved tropospheric HCHO columns.

5.4 Error budget for the HCHO column

An estimation of the error budget for the GOME-2 HCHO column is provided in Table 6. This includes typical errors on the HCHO slant columns and the AMF. As discussed above, AMF errors are difficult to quantify since depending on the HCHO profile, clouds may shield a major part of the HCHO column from the GOME-2 view. The AMF error in Table 6 has been estimated for cloud free conditions, and hence this error will be larger for cloudy conditions. A detailed description of the different error sources in the HCHO retrieval from GOME-2 is given in De Smedt et al. (2012).

Table 6 Estimation of error sources for the HCHO column.

Error source	Percent error
HCHO slant column	10 – 20
HCHO absorption cross-sections	5 – 10
Other (Instrument signal-to-noise, Ozone abs. interference, Ring effect)	5 – 10
HCHO Reference Sector Correction	5-10
HCHO Air Mass Factor	10 – 20
HCHO vertical column (accuracy)	25 – 50

6 THE SO$_2$ COLUMN ALGORITHM

The two main sources for atmospheric SO$_2$ are anthropogenic pollution and natural sources, mainly from volcanic eruptions. The main challenge of the SO$_2$ retrieval is the unknown height of the SO$_2$ layer in the atmosphere which can range from the ground up to the stratosphere, depending on the type of emission. The SO$_2$ retrieval algorithm consists of two main parts: The retrieval of the slant column densities from L1 data using the DOAS method and the conversion to total vertical columns by means of an Air Mass Factor. In order to represent a set of different SO$_2$ emission scenarios, four different AMFs are calculated and hence four different vertical columns can be found in the L2 product.

Three scenarios for volcanic emissions are represented by the SO$_2$ "plume" height assumed for the calculation of the AMF:
- At an altitude of 2.5 km a.s.l. (at about 760 hPa), representing the plume height of passive degassing of low volcanoes.
- At an altitude of 6 km a.s.l. (at about 500 hPa) representing the plume height of effusive volcanic eruptions or passive degassing of high volcanoes
- At an altitude of 15 km a.s.l. (at about 140 hPa), representing the plume height of explosive eruptions.

The scenario representing anthropogenic SO$_2$ emissions is represented by an AMF calculated for a typical polluted boundary layer SO$_2$ profile (see Sect. 6.2).

A description of the different SO$_2$ retrieval steps in the GDP 4.8 algorithm is given below.

6.1 DOAS slant column fitting

The DOAS algorithm for SO$_2$ (Rix et al., 2009, 2012) is based on the DOAS algorithm for ozone, as described in Sect. 2.2. The DOAS algorithm settings for SO$_2$ are listed below:

- The DOAS slant column fit of SO$_2$ is performed in the UV wavelength range 315-326 nm (Thomas et al., 2005).
- A single SO$_2$ cross-section is included in the fit, the SO$_2$ cross-sections are the SCIAMACHY Flight Model cross-sections from Bogumil et al. (2003) for a temperature of 203K, reconvolved with the GOME-2 slit function (GOME-2A: Flight Model 3, GOME-2B: Flight Model 2) (Siddans et al., 2006, 2012).
- Cross-sections of the interfering trace gases O$_3$ and NO$_2$ are included. The best results in this wavelength region are obtained using the Brion/Malicet ozone cross-sections (Malicet et al., 1995; Brion et al., 1998) at two temperatures (218K and 243K) with a pre-shift of -0.01 nm; for NO$_2$, the GOME-2 Flight Model/CATGAS cross-sections is used at 241K (Gür et al., 2005).
- In order to account for the strong ozone absorption in the SO$_2$ fitting window and the interference between the SO$_2$ and O$_3$ absorption features, two additional fitting parameters are included in the DOAS analysis (Puķīte et al., 2010). Here, the O$_3$ slant columns as function of wavelength and optical depth are described by Taylor series. The Taylor coefficients provide two additional cross-sections for O$_3$ at 243K (original cross-section multiplied by wavelength and original cross-section squared).
- Two Ring reference spectra calculated with the SCIATRAN model are included as additive fitting parameters to account for the molecular ring effect (Rozanov et al., 2001).
- Intensity offset effects that may be induced by residual stray-light or remaining calibration issues in the level-1 product are known to be sources of bias in DOAS retrievals of minor trace species. To correct for this, a linear offset correction is used by including an inversed solar irradiance spectrum as additional effective cross-section in the DOAS fit. The broadband filtering polynomial is of 5th degree.

6.1.1 Slant column corrections

After the DOAS retrieval, two corrections are applied on the SO_2 slant columns:

<u>SO_2 background correction</u>
The atmospheric background level of SO_2 is in general very low. In order to account for any systematic bias in the retrieved SO_2 column and to ensure a geophysical consistency of the results, a background correction is applied to the data to avoid non-zero columns over regions known to have very low SO_2 and at high solar zenith angles. When retrieving SO_2 slant columns from satellite data without using the Puķīte et al. (2010) approach for the treatment of ozone, one generally observes negative SO_2 slant column results towards high latitude. This is the result of an enhanced relative contribution of ozone to the total absorption along the slant path for large solar zenith angles. In previous versions of the GDP, we therefore applied a parameterized correction to compensate for artificial background levels of SO_2.

With the use of the additional pseudo ozone cross-sections as described in the previous section, the need for a correction as function of solar zenith angle is less important, and therefore a background correction scheme based on latitude and surface height is used in the GDP 4.8. This offset is calculated on a daily basis for latitude bands of 2 degree width. Furthermore, the offset values are separately calculated for 5 different surface altitude bins. In order to minimize the effect of outliers or missing data in the daily dataset, a median offset value based on the offset values calculated for the last two weeks before the day of interest is finally calculated. This latitude and altitude dependent value is finally subtracted from the SO_2 slant column densities.
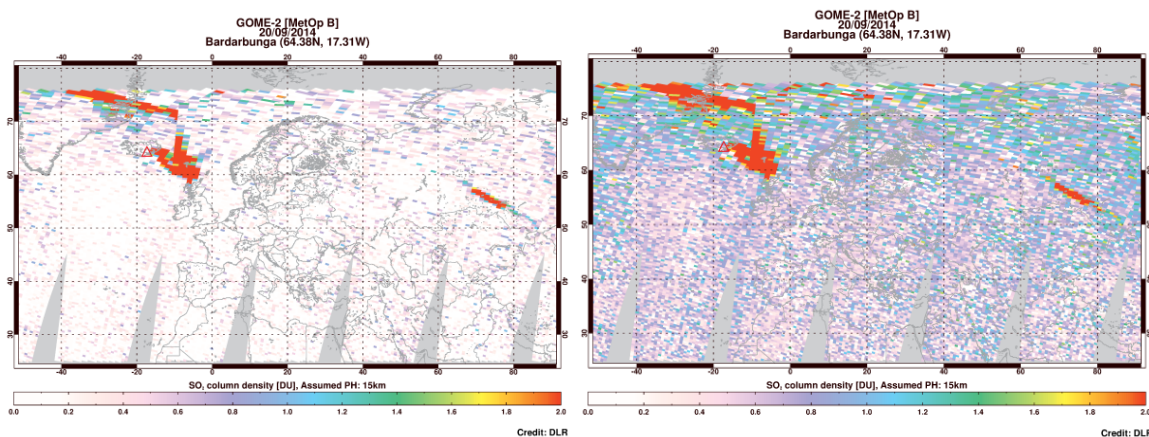

Figure 12   Effect of the background correction. The left image shows the background-corrected SO_2 vertical column during the Bardarbunga eruption on 20 September 2014, whereas on the right image the correction is not applied.

<u>SO_2 temperature correction</u>
The SO_2 absorption cross-sections show a dependence on temperature. In the atmosphere the temperature is mainly a function of height, therefore cross-sections at different temperatures should be used for the different plume heights and anthropogenic pollution scenario assumed in the GOME-2 retrieval. The simplest approach to correct for the temperature dependence is to calculate a scaling factor for the dependence using a linear least-squares fit. In the SO_2 fitting window the scaling coefficients show a linear dependency which allows that the slant column retrieval can be performed only once with a fixed cross-section temperature and can be corrected to the atmospheric temperature for the respective scenario:

$$S_T = \frac{S_{T0}}{1 - \alpha(T - T_0)} \qquad (24)$$

Here, S_{T0} is the SO$_2$ slant column retrieved using a cross-section at a temperature of T_0= 203K. α is the scaling factor, which was found to be α = 0.003, and T is the atmospheric temperature, which is set to 203K, 243K, 273K and 283K for the 15km, 6km, 2.5 km plume height and anthropogenic pollution scenario, respectively. The error associated to the assumption of a single temperature for each plume height ranges from <5% (at 15 km) to about 10% for the PBL (taking into account the range of temperature found at the four assumed heights). This is a relatively small error source in relation to the total error in the SO$_2$ vertical column (see also Sect. 6.3).

6.2   AMF and VCD determination

For the conversion from the slant column to a vertical column an Air Mass Factor (AMF) is used, which is complicated by the strong dependence on clouds, aerosols, and most importantly, on the *a priori* vertical profile of SO$_2$ in the atmosphere (see Figure 13). Especially the different emission sources of SO$_2$ (volcanic emissions at different altitudes, as well as anthropogenic emissions in the PBL), should be taken into account in the AMF calculations.

For the volcano scenarios, a volcanic SO$_2$ profile is assumed with a predefined central plume height (15, 6 and 2.5 km) with a Gaussian profile shape. For each of the three volcano scenarios, the AMF is calculated with the LIDORT model according to Eq. (2) for the fitting window mid-point (320 nm). The surface albedo is obtained from the combined TOMS/GOME climatology (Boersma et al, 2004), see Sect. 2.3.5. The computation of the SO$_2$ vertical column density proceeds then via:

$$V^{(n)} = \frac{S^{(n)}}{(1-w)M_{clear}^{(n)} + wM_{cloud}^{(n)}}$$ (25)

Where (n) denotes the scenario, S the background- and temperature corrected SO$_2$ slant column, M_{clear} and M_{cloud} the clear-sky and cloudy AMF, respectively and w the intensity-weighted cloud-fraction (see Eq. 4). Clouds are treated using the independent pixel approximation (IPA), i.e. clouds are treated as Lambertian reflecting surfaces and for the AMF calculation the cloud top albedo and cloud top pressure is used. No ghost column correction is applied for the SO$_2$ retrieval.

AMF calculations for the anthropogenic SO$_2$ scenario use an average SO$_2$ profile with a total column of 0.37 DU, which is based on aircraft measurements from 2000 to 2005 (Taubmann et al. 2006). The computation of the SO$_2$ vertical column density for the anthropogenic scenario proceeds then with Eq. (25). Since the cloud-top pressure output is highly unstable for low effective cloud fractions (<30%) a clear-sky AMF (i.e. the cloud fraction is set to 0) is used.

6.3 Error budget for the SO$_2$ column

An error estimate of the retrieved SO$_2$ column from GOME-2 is given in Table 7. This includes typical errors on the SO$_2$ slant column and the AMF for the volcanic and anthropogenic emission scenarios. AMF errors are difficult to quantify since depending on the volcanic scenario or anthropogenic scenario, clouds may shield a major part of the total SO$_2$ column from the GOME-2 view in case they are located above the SO$_2$ plume or may even enhance the retrieved SO$_2$ column when they are located below.
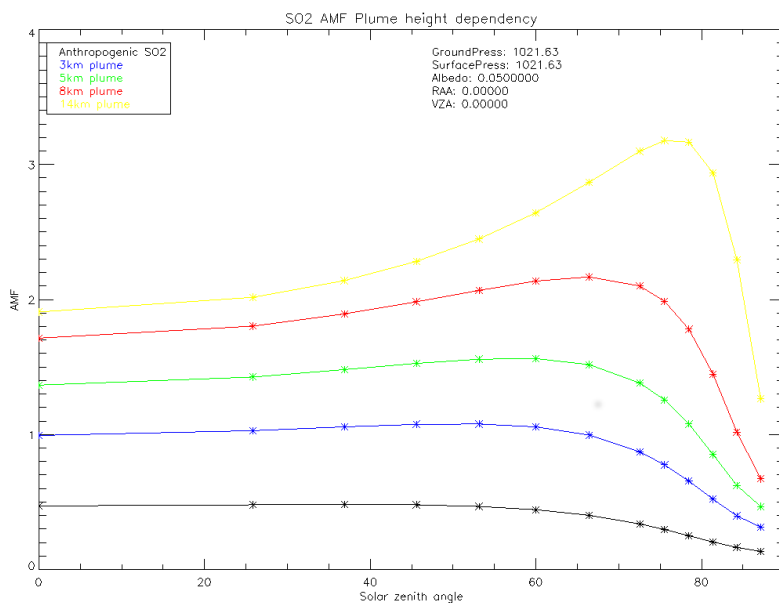
Figure 13 Dependence of the SO_2 Air Mass Factor on the assumed volcanic or anthropogenic emission scenario. The AMF has been calculated as a function of solar zenith angle for clear-sky nadir viewing conditions and surface albedo 0.05. The assumed total SO_2 column for the volcanic scenarios is 3 DU.

.

Table 7 Estimation of error sources for the total SO_2 column.

Error source	Percent error
SO_2 slant column	30 – 50
SO_2 absorption cross-sections	10 – 15
Atmospheric (effective) temperature	5 – 10
Other (Instrument signal-to-noise, Ozone abs. interference, Ring effect)	20 – 30
SO_2 Air Mass Factor	20 – 50
SO_2 vertical column (accuracy)	50 – 100

6.4   Volcano activity detection

A new algorithm has been implemented in the GDP 4.8 in order to identify elevated SO_2 values from volcanic eruptions. It is based on the GOME-2 volcanic SO_2 detection algorithm described in Brenot et al. (2014) and was further developed to identify the entire volcanic SO_2 plume, as explained below.

When an SO_2 vertical column is exceeding a certain threshold value it is checked whether at least half of the neighboring GOME-2 measurements within a distance of 90 km (measured from the GOME-2 ground-pixel center) also exceed this threshold value. In this way, elevated SO_2 columns from volcanic eruptions are discriminated from anthropogenic pollution and from pure noise. Four different SO_2 threshold values based on the position (Latitude/Longitude) of the pixel are discriminated:

- Currently a general background threshold of 1.2 is used
- Within a radius of 300 km to known volcanoes the threshold is 0.7 DU.
- In regions with known anthropogenic SO_2 sources the threshold is 2 DU.
- In the South Atlantic Anomaly (SAA) region as well as for high solar zenith angles (>70deg), the threshold is set to 3 DU. Within this region at least two-thirds of the neighboring pixels have to fulfill this threshold criterion.

Furthermore the threshold on the SO_2 error should be less than 50%.

The volcano activity indicator is stored as a flag in the GOME-2 L2 product (Valks et al., 2014) that can adopt the following values:
- 0: No elevated SO_2 value
- 1: Elevated SO_2 value due to a volcanic SO_2 plume
- 2: Elevated SO_2 value in a region with known anthropogenic emissions
- 3: Elevated SO_2 value in the SAA region or for high SZA (>70deg)

All GOME-2 measurements within the given distance of 90 km that also exceed the selected thresholds are assigned either the same flag value (or a higher flag value if already set).
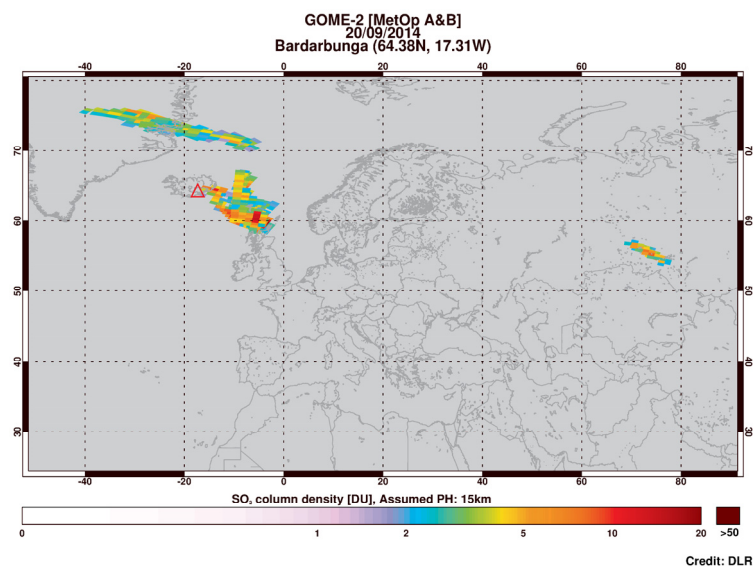

Figure 14   GOME-2 SO_2 measurement of the Bardarbunga volcanic eruption on 20 September 2014. Only data flagged by the volcano activity detection algorithm is plotted, clearly showing the location of the SO_2 clouds.

7 THE H_2O COLUMN ALGORITHM

7.1 DOAS slant column fitting

The DOAS algorithm for H_2O (Grossi et al., 2015) is based on the DOAS algorithm for ozone, as described in Sect. 2.2. The DOAS algorithm settings for H_2O are listed below:

- The fitting window is 614-683.2 nm in GOME-2 Channel 4. H_2O absorption features are prominent, and GOME measurements have high signal-to-noise and small interference effects.
- A single H_2O cross-section reference spectrum is used. This is based on line-by-line computations using HITRAN (Rothman et al., 2005) H_2O line parameters at 290K, followed by a GOME-2 slit function convolution. There is no retrieval of an effective temperature; the temperature dependence is relatively small, and saturation issues of the cross-sections are accounted for on the AMF level (see below).
- O_2-O_2 and O_2 are interfering species and the respective cross sections are included in the fit. Sources are Greenblatt et al. (1990) for O_2-O_2 and HITRAN (Rothman et al., 2005) for O_2 (the latter as input to line-by-line computations, for an effective atmospheric temperature of 290K, which are followed by GOME-2 slit function convolution).
- There is one additive Fraunhofer Ring spectrum for this region of Channel 4; a molecular Ring correction is not applied.
- Intensity offset effects that may be induced by residual stray-light or remaining calibration issues in the level-1 product are corrected by fitting the inverse of the sun spectrum as another effective cross-section.
- The broadband filtering polynomial is 4th order (5 coefficients).
- Three types of vegetation spectra are included in the fit to improve the broadband filtering. These are also included over water, as marine chlorophyll-containing substances may show similar spectra.

The H_2O absorption lines are much narrower than the GOME-2 resolution. After traversing the atmosphere and subsequent folding with the instrument slit function, saturation effects in the strongest lines lead to a difference with the case where a similar line profile at GOME-2 resolution would have traversed the atmosphere (the latter is the DOAS assumption). This effect has been numerically modelled by Wagner et al. (2003), see Figure 15.

In the GOME-2 Level 2 H_2O product (see Valks et al. (2014)), the uncorrected SCD obtained from the DOAS fit is provided. The modelled saturation correction is then applied in the conversion from SCD to VCD, in conjunction with the modelled AMF (see below).

In addition to the saturation effect, there is also a temperature dependence of the H_2O cross sections. The error made by assuming one fixed temperature for the whole atmosphere has been assessed by Wagner et al., (2003); they derive an error of ±3%.
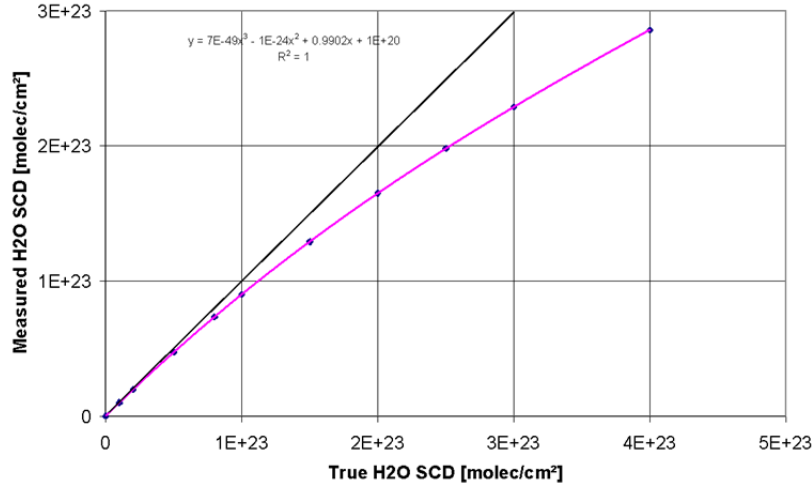
	REFERENCE:	**SAF/AC/DLR/ATBD/01**
	ISSUE:	3/A | Rev. 2
	DATE:	27.06.2017
	PAGE:	52

EUMETSAT
AC SAF
ATMOSPHERIC COMPOSITION
MONITORING

Figure 15   Relation between "true" H_2O slant column from a line-by-line modelling, and the "measured" H_2O slant column derived from a fit of the DOAS cross sections to the GOME-convolved absorption spectrum. Dots represent the calculations; the pink line is the polynomial fit from Eq. (27) - the black line indicates equality.

7.2 AMF and VCD determination

For all trace gases which are mainly present in the troposphere, the conversion from the slant column to a vertical column is complicated by the strong dependence of the Air Mass Factor on clouds, aerosols, surface albedo, and on the *a priori* vertical profile of the trace gas in the atmosphere (e.g. Richter and Burrows, (2002)). The situation may be improved by using a "measured AMF" derived from the slant column of an absorber with "known" VCD (Noël et al., 1999). In the case of H_2O, we can use the slant column of O_2, which is fitted simultaneously from the same DOAS fitting window. The usual formula $VCD_{H2O} = SCD_{H2O} / AMF_{H2O}$ may then be rewritten as:

$$VCD_{H2O} = \left(SCD_{H2O,corr} / SCD_{O2,corr}\right) \cdot VCD_{O2} \cdot AMF\_ratio(SZA, LOS, RAz, Alb) \tag{26}$$

In this formula the SCD_{corr} denote slant columns which have been corrected for the saturation effect. For H_2O, this is calculated as:

$$SCD_{H2O,corr} = 1.51196 \cdot 10^{-24} \cdot SCD_{H2O}^2 + 0.962779 \cdot SCD_{H2O} + 5.17495 \cdot 10^{20} \tag{27}$$

where SCD_{H2O} denotes the (uncorrected) slant column for H_2O obtained from the DOAS fit.
For O_2, the saturation correction is given by:

$$SCD_{O2,corr} = 1.0063790 \cdot 10^{-51} \cdot SCD_{O2}^3 + 2.5049862 \cdot 10^{-26} \cdot SCD_{O2}^2 + $$
$$0.94507654 \cdot SCD_{O2} + 1.0617513 \cdot 10^{23} \tag{28}$$

where SCD_{O2} denotes the (uncorrected) DOAS slant column for O_2.

The factor *AMF_ratio(SZA,LOS,RAz,Alb)* accounts for differences between the AMF of H_2O, and the AMF of O_2, due to the different vertical profiles of these trace gases. This ratio is strongly dependent on solar zenith angle (SZA), see Figure 16, on surface albedo (*Alb*), see Figure 17, and to a lesser extend on line-of-sight (LOS) and relative azimuth (RAz) angles.
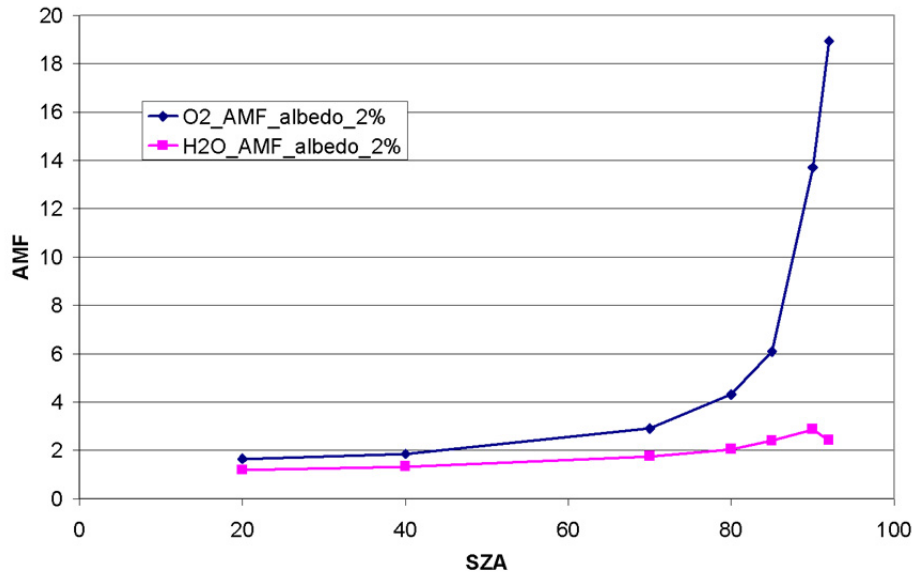
Figure 16   Dependence of the H_2O and O_2 Air Mass Factors on solar zenith angle for clear-sky nadir viewing conditions and a surface albedo of 0.02.
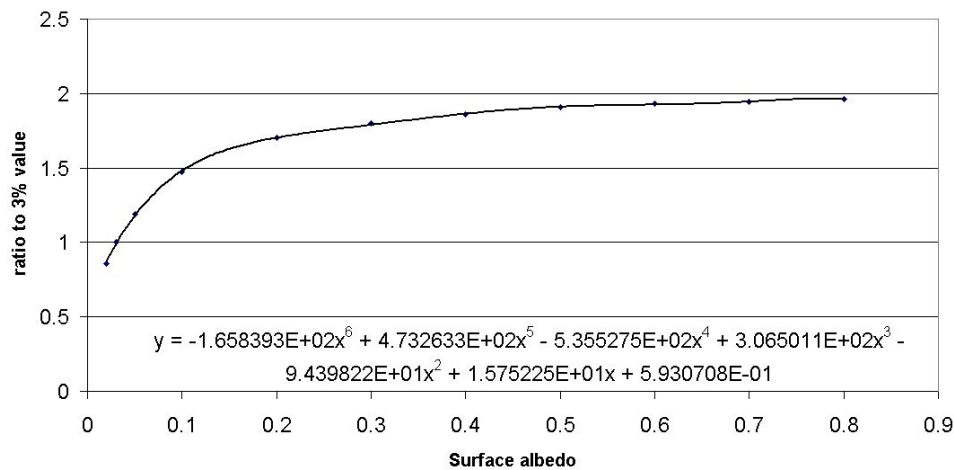

Figure 17   Dependence on Albedo of the ratio of Air Mass Factors of H_2O and O_2, this is the variable denoted *Albedo_ratio* in the text.

The dependence on surface albedo has been investigated by T.Wagner (MPI-C) in the framework of the ESA DUE GlobVapour project. Albedo dependence may be factorised out of the dependence on geometry:

$$AMF\_ratio(SZA, LOS, RAz, Alb) = AMF\_ratio\_geo(SZA, LOS, RAz) / Albedo\_ratio \tag{29}$$

where *AMF_ratio_geo(SZA,LOS,RAz)* is a lookup table, calculated for a surface albedo of 3%, and *Albedo_ratio* is a polynomial which describes the ratio of the AMFs for the actual surface albedo, w.r.t. to the 3% albedo used for the lookup table:

$$\begin{aligned} Albedo\_ratio \quad = \quad &-165.8393 \cdot Alb^6 + 473.2633 \cdot Alb^5 - 535.5275 \cdot Alb^4 + 306.5011 \cdot Alb^3 \\ &-943.9822 \cdot Alb^2 + 15.75225 \cdot Alb + 0.5930708 \end{aligned} \tag{30}$$

where the surface albedo *Alb* is taken from the database from Grzegorski (2009), except over water, where a fixed albedo of *Alb* = 0.03 is used. For high latitudes (>50°), where the database of Grzegorski has no values, data from Koelemeijer et al. (2003) are taken.

The differences between the AMF of H_2O, and the AMF of O_2, are also dependent on the exact tropospheric profile of H_2O, and, most importantly, on cloud cover - but these dependencies are currently neglected. However, a cloud flag is included in the Level 2 H_2O product, which is set when cloud cover invalidates the AMF model (see below).

In the GOME-2 Level 2 product, the H_2O total column is reported in units of kg/m^2. The conversion factor from molec/cm^2 to kg/m^2 is $2.9915 \cdot 10^{-22}$.

7.3 Cloud flagging for the H_2O column

Two separate cloud contamination indicators are used. In the first case, clouds are inferred from an anomalously high surface reflection. The cloud flag is set if the product of cloud fraction and cloud albedo (derived from the OCRA and ROCINN algorithms, see Chapter 0) exceeds 0.6 – in this case also the H_2O total column is set to 'invalid' as the pixel may be considered as "fully" clouded. The second cloud indicator is derived from the fitted O_2 DOAS slant column, as cloud cover reduces the observed column of O_2. This H_2O cloud flag is set if the O_2 slant column is smaller than a pre-calculated value from a lookup table, dependent on SZA and LOS (roughly when 20% from the column to ground is missing, for a discussion of this limit see Wagner et al. (2006)). Each cloud flagging has limitations: the method using the surface reflection may flag cloud-free pixels with snow or ice surface, while the method using the O_2 column will not detect low clouds (cloud top height below ~2 - 3 km).

7.4 Empirical Correction for scan angle dependency in the GOME-2 H_2O column

The quality of the GOME-2 H_2O column product is affected by the dependency of the H_2O columns on the instrument viewing angle geometry. The scan angle dependency of the GOME-2 H_2O columns is very similar for MetOp-A and MetOp-B. An analysis of the water vapour columns data revealed a systematic scan angle dependency (SAD) already in the H_2O slant column density results (Grossi et al., 2015). We observed different SADs over land and sea, and a particularly strong effect for cloud free pixels over sea areas, which suggested a correlation between the simplified Lambertian assumption used to describe the Earth reflectivity and the SAD. We found that using a simple Lambertian approach and ignoring the Bidirectional Reflectance Distribution Function, we underestimate the Air Mass Factor over ocean in the East Region of the scan (and overestimate it in the West Region) by up to 30%.

In the GDP 4.8, we implemented two distinct empirical corrections for the scan angle dependency over land and over sea, to take into account the different reflectivity of the surface. The respective correction factors were determined from a 6 years time-series of GOME-2/MetOp-A measurements (2007-2012). We used scan angle read-outs toward the middle ground pixel as reference values to normalize the H_2O total column for every forward scan angle position and employed only regions with a large number of measurements to avoid natural variability. We fitted a polynomial to the normalized measurements in order to remove outliers and obtain a smooth correction function. Outside of the valid latitudinal range we interpolated between the last valid value and 1 (i.e. no correction) for +/- 90° latitude, as done for ozone (Sect. 2.5). In the GDP, look-up tables of polynomial fitting parameters with the scan angle correction dependent on month, latitude and scan angle have been implemented. Figure 18 shows the empirical correction factors as a function of latitude and scan angle for the month of May for land and sea.
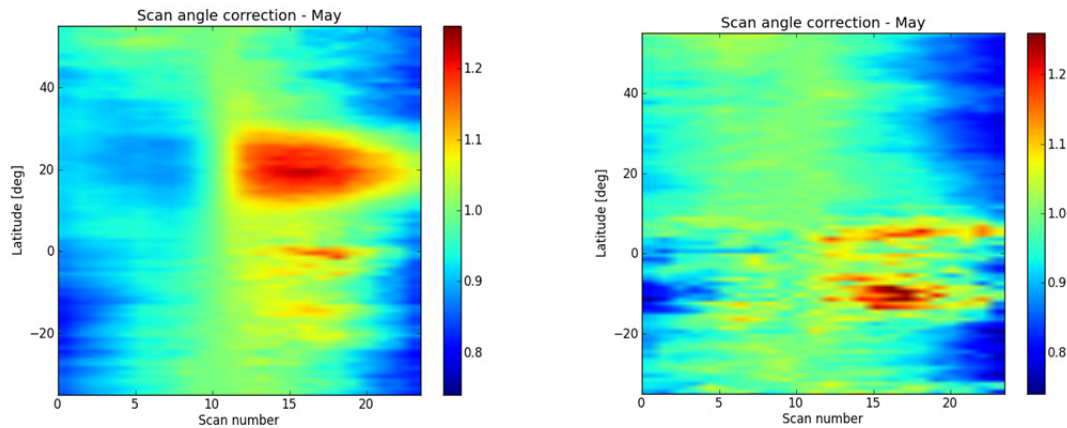
Figure 18   Empirical scan angle correction factors for the GOME-2 H_2O columns as function of latitude and pixel index within the scan (0=East; 23=West) for May. We computed two distinct empirical corrections for the scan angle dependency over land (left) and over sea (right).

In the left and right panel of Figure 19 one can distinguish the GOME-2A water vapour VCD before (solid line) and after (dashed line) applying the empirical correction for the scan angle dependency. The different lines refer to latitudinal averaged quantities in the northern, tropical and southern hemisphere regions for January 2013. Note that while in austral summer (Dec-Feb), the correction is larger for 20° - 50^oS (see Fig. 19), in the Northern Hemisphere summer months (Jun-Aug), it is larger for 20° - 50^oN.
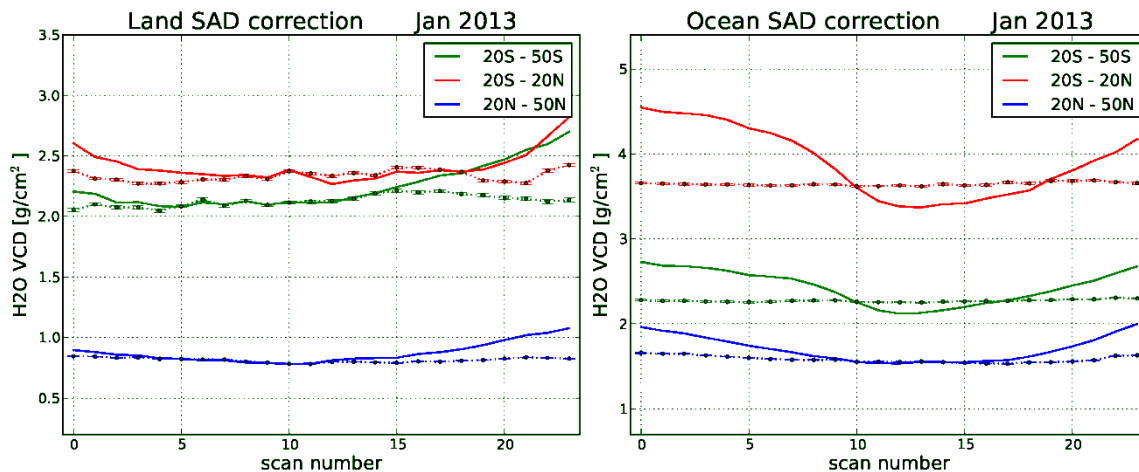

Figure 19   GOME-2A H_2O VCD as a function of pixel index within the scan (0=East, 24=West) averaged in different latitude bands (20ºS - 50ºS, 20ºS - 20ºN, 20ºN - 50ºN) before (solid line) and after (dashed line with points) the scan angle dependency correction for January 2013. We show separately the empirical correction applied over land measurements (left panel) and over ocean measurements (right panel).

7.5 Error calculation for the H$_2$O column

The error on total column of H$_2$O is calculated as:

$$\varepsilon\_H2O = \sqrt{\left(\varepsilon\_SCD_{H2O}\right)^2 + \left(\varepsilon\_SCD_{O2}\right)^2 + \left(\varepsilon\_general\right)^2 + \left(\varepsilon\_AMF\right)^2} \tag{31}$$

Where ε_SCD_{H2O} and ε_SCD_{O2} are the DOAS fit errors for the slant columns of H$_2$O and O$_2$, respectively. $\varepsilon\_general$ is a general error contribution (e.g. cross-section, temperature, Ring effect etc.) taken as a constant of 10%. ε_AMF is an uncertainty for the radiative transfer, including cloud effects, which is calculated as $\varepsilon\_AMF = \left(SCD_{O2} - SCD_{O2,\max}(SZA) * 1.16\right)/2 \cdot 10^{25}$. This error increases with decreasing O$_2$ slant column (indicating strong cloud shielding). From sensitivity studies (e.g. Wagner et al., 2006) it was shown that for measurements with low O$_2$ slant column, the retrieved H$_2$O vertical column systematically underestimate the true H$_2$O column.

7.6 Error budget for the H$_2$O column

An estimation of the error budget for the H$_2$O slant column (without saturation correction), and for the H$_2$O total column, is provided in Table 8. The slant column error estimates are mainly based on the DOAS analyses using GOME data (Wagner et al., 2003).

The errors on the AMFs are difficult to quantify, as there may be compensating effects. E.g., high surface reflectivity as in the case of snow would lead to a much lower AMF-ratio of O$_2$ to H$_2$O - but above cold surfaces the tropospheric column of H$_2$O is reduced, which has the opposite effect. The combined error can therefore be smaller than the error on each parameter separately. Preliminary AMF error estimates for clear sky are based on model calculations of various scenarios.

Clouds may shield a major part of the total H$_2$O column from the GOME-2 view. This effect is partly compensated for by using the "measured" AMF of O$_2$, but errors remain which depend on cloud properties and on H$_2$O vertical distribution. In the GDP, cloud contamination is taken into account in the calculation of errors on H$_2$O column, and cloudy conditions are flagged.

Table 8 Estimation of error sources for the total H$_2$O column.

Error source	Percent error
H$_2$O slant column	
H$_2$O absorption cross-sections	< 5
Atmospheric (effective) temperature	3
Other (Instrument signal-to-noise, interference, Ring effect)	< 3
H$_2$O Air Mass Factor	
Clear Sky	10 – 25
Cloudy	20 – 100
H$_2$O vertical column (accuracy)	15 – 100

8 THE OCIO COLUMN ALGORITHM

In order to understand and track the development of stratospheric ozone, both ozone levels and the amounts of ozone depleting substances need to be monitored. In this context, GOME-2 observations can contribute with measurements of BrO (see Chapt. 4) and OClO in the stratosphere. The latter is formed by reaction of ClO and BrO and can thus provide indirect information on ClO levels. UV-visible satellite measurements of OClO are performed by applying absorption spectroscopy in the 330 – 390 nm spectral region where the molecule exhibits characteristic absorption structures. These OClO observations are focused on stratospheric applications and GOME-2 can detect OClO only when ClO is activated. As OClO photolyses rapidly, it can only be observed at large solar zenith angle, usually during twilight. Due to the sphericity of the Earth's atmosphere, the solar zenith angle changes along the light path from the sun to a point in the atmosphere, making the signal a complex mixture of the vertical OClO profile, its change with Solar Zenith Angle and the light path. Therefore, the OClO slant columns as measured by GOME-2 are not converted to vertical columns.

In spite of its very characteristic absorption features, the retrieval of OClO from GOME-2 is difficult for several reasons. First of all, signals at low sun are small and therefore the signal to noise ratio is relatively poor. Second, depending on fitting window used, the ozone absorption can present a significant interference, and in addition has a large temperature dependence. Lastly, the ozone retrieval has proven to often have offsets, leading to positive or even negative columns in the absence of atmospheric OClO. These problems are present in all OClO retrievals. For GOME type instruments, lv1 calibration issues have shown to pose additional challenges.

Using retrieval settings similar to those applied for SCIAMACHY, a demonstrational OClO product has been developed for GOME2-A in 2009, which reproduced the overall pattern of chlorine activation. However, a validation by Richter et al. (2009) revealed that there were many problems in the GOME-2 OClO data outside the regions of chlorine activation, leading to seasonal biases, sea-land contrast, cloud effects and scan angle dependencies. Furthermore, the scatter in the GOME-2 OClO data was very large in comparison to SCIAMACHY (and GOME-1).

In 2015, an improved OClO retrieval algorithm for both GOME-2A and -B has been developed by Richer et al. (2015) within the framework of an O3M SAF Visiting Scientist project (VSA ID O3_AS14_02). A detailed description of the improved OClO retrieval algorithm, an analysis of the time evolution and offsets in the GOME-2 OClO columns, and an initial validation with ground-based OClO measurements are given in the Visiting Scientist report (Richter et al., 2015).

In the next Section, the improved OClO slant column retrieval using the DOAS method is described and in Sect. 8.2, the normalization and offset correction of the GOME-2 OClO columns is discussed. An error assessment of the GOME-2 OClO columns is presented in Sect. 8.3

8.1 DOAS slant column fitting

The improved algorithm for the OClO retrieval from GOME-2 is based on the DOAS analysis by Richter et al., 2015. The DOAS algorithm settings for OClO for GOME-2A and –B are listed below:

- The DOAS slant column fit of OClO is performed in the UV wavelength range 345-389 nm.
- A single OClO cross-section is included in the fit, the OClO cross-section is from Kromminga et.al (2003) for a temperature of 213 K and a resolution of 20 cm^{-1}.
- Cross-sections of the interfering trace gases O_4, O_3 and NO_2 are included. The best results in this wavelength region are obtained using the Hermans et al. [1999] O_4 cross-section. For O_3 and NO_2, the GOME-2 FM3 and FM2 cross-sections are used [Gür et al., 2005]. Two ozone cross-sections for 223 and 243 K are included, and a single NO_2 cross-section at 223K.
- Furthermore a Ring reference spectrum, calculated with the SCIATRAN model in an $O_2/N_2/O_3$ atmosphere at 10% surface albedo and 30° SZA, is included as additive fitting parameter to account for the Ring effect.

- The absorption cross-sections are convolved with the GOME-2 slit function (Siddans et al., 2006, 2012).
- To correct for intensity offset effects that may be induced by residual stray-light or remaining level-1 calibration issues, a linear offset correction with an inversed earth-shine spectrum as additional effective cross-section is used.
- The broadband filtering polynomial is 4th order (5 coefficients).
- As correction for residual polarization errors in the level-1 product, the GOME-2 keydata parameter Eta (EUMETSAT, 2011) is fitted as another effective cross-section. Including Eta significantly improves the fitting residuals of the OClO fit in the large 345-389 nm fitting window.
- Two empirical correction functions (derived from mean DOAS-fit residuals) are included as additional (pseudo-) absorption cross-sections in the DOAS-fit for GOME-2B: a mean residual and a scan angle correction function. These two empirical functions correct for positive off-sets and scan angle dependences in the OClO columns for GOME-2B. DOAS fit analysis showed that for GOME-2A, only the empirical scan angle correction function needs to be taken into account in the DOAS fit (including the mean residual correction function does not improve the OClO columns from GOME-2A). The calculation and use of the empirical correction functions is described in detail in the OClO Visiting Scientist report (Richter et al., 2015).

Figure 20 shows the time evolution of the OClO slant columns from GOME-2A (2007-2015) and GOME-2B (2013-2015) for different latitude bands on the Southern Hemisphere (over the Pacific sector). Ideally, all values should be close to zero with the exception of the high latitude regions during chlorine activation. GOME-2B OClO slant columns at latitudes smaller than 50° have values always below $2x10^{13}$ molec cm^{-2}. For the 60°-70° bins variability is much larger, in particular in the Southern Hemisphere due to irregular movements of the vortex bringing activated air masses in and out of the reference region. Figure 20 shows that for GOME-2A, there is a clear downward trend in overall values in the first years of operation, most notable in the year after the second throughput test in September 2009. From 2011 onwards, data seems to be more stable. Furthermore, the seasonal variation for the low and mid-latitude bins is much larger than in GOME2-B data, in particular in the first years. The amplitude of this seasonality is strongly reduced after 2010.

As can be seen in Fig. 20, a sudden jump in offsets by about $5x10^{13}$ molec cm^{-2} is observed at all latitudes after 25 June 2015 for both GOME-2A and GOME-2B (but in opposite directions), which is related to a update of the GOME-2 Lv1 processor version (to PPF 6.1). For GOME-2B, this offset can be reduced by using updated empirical correction functions (derived from DOAS-fit residuals from GOME-2 measurements after 25 June 2015).

8.2 Normalisation and offset correction

With the updated DOAS algorithm described above, the quality of the GOME-2 OClO columns is clearly improved compared to the demonstrational results based on the original algorithm from 2009, especially for the GOME-2B instrument. However, an additional offset correction is needed to correct for remaining biases in the OClO columns (e.g. non-zero OClO columns over areas without chlorine activation), the temporal drifts observed mainly in the OClO data from GOME-2A (see Fig. 20 and Richter et al., 2015). To that end, a simple but effective normalization is applied on an orbital basis. The mean OClO slant column for the area between 50°N and 50°S (a latitude region without chlorine activation) is determined for each GOME-2 orbit, which is then subtracted from the retrieved OClO slant columns for the complete orbit.

This normalization method also effectively corrects for the sudden jump in the OClO columns after 25 June 25 2015 related to the change in the lv1 processor version (to PPF 6.1) for both GOME-2 instruments.

As mentioned above, OClO can only be observed at large solar zenith angle and under these circumstances the calculation of an AMF and a vertical column is not useful. Therefore, the GOME-2 data product will only contain (corrected) slant columns of OClO, not vertical columns as for the other trace gases.

In addition, the noise (random error) in the OClO slant columns is large (see also next section), and the GOME-2 measurements are normally not interpreted individually. Averaging over time or in space is needed to derive meaningful OClO values.

8.3 Error budget for the OClO column

The error on the OClO retrieval is dominated by instrument noise and systematic errors. The retrieval error is estimated to be ~2.10^{13} molec/cm^2 under good illumination conditions, but will increase rapidly as illumination decreases. At the same time OClO slant columns are expected to strongly increase (with solar zenith angles above 90°). Under activated conditions, relative errors in OClO slant columns below 50% are targeted.
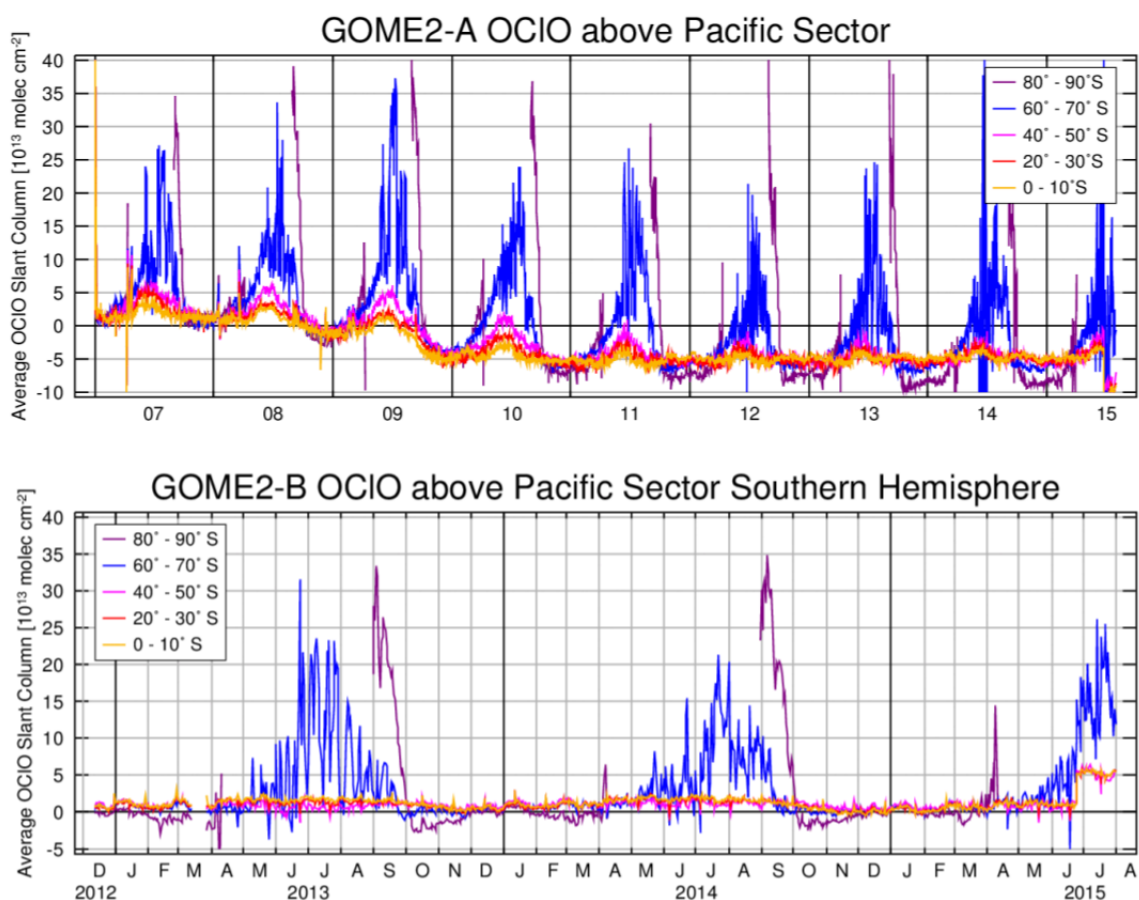

Figure 20 Time evolution of (top) GOME2-A and (bottom) GOME-2B OClO slant columns (without offset correction) for different latitude bands for the Southern Hemisphere (over the Pacific sector).

9   CLOUD ALGORITHMS

GOME-2 footprints are comparably large and the retrieval is often affected by partially cloudy scenes. In such cases, the tropospheric contribution of trace species below clouds to the total content must be taken from climatological trace gas databases. Furthermore, clouds are quite opaque in the GOME spectral range and consequently, in the cloudy portion, the cloud-top can be considered as the effective lower reflecting boundary of the earth-atmosphere system, relative to the top of atmosphere. It is therefore vital to know the cloud fraction, the cloud-top height and cloud-top albedo parameters for providing reliable trace gas columns. These three parameters are needed for the computation of the cloudy and total AMF used to calculate the VCD of the GOME-2 trace gases (e.g. Eq. (5) and (15)), and the ozone ghost column.

Two algorithms OCRA and ROCINN (Loyola et al., 2007; Lutz et al., 2016) are used for generating GOME-2 cloud information inputs for the trace gas column retrievals: OCRA for cloud fraction, and ROCINN for cloud-top height (pressure) and cloud-top albedo (optical thickness).

9.1 OCRA cloud fraction algorithm

The basic idea in OCRA (Optical Cloud Recognition Algorithm (Loyola and Ruppert, 1998) is to break down each optical sensor measurement into two components: a cloud-free background and a residual contribution expressing the influence of clouds. The key to the algorithm is the construction of a cloud-free composite that is invariant with respect to the atmosphere, to topography and to solar and viewing angles. For a given location (x,y), we define a reflectance $\rho(x,y,\lambda)$ measured by the PMDs of GOME-2 at wavelength range λ for the ground cover projection of the image. The PMD reflectance is corrected for instrumental degradation as well as for scan angle dependencies and latitudinal dependencies. The degradation correction is empirical. For each polarization and color RGB, a time-series of daily mean reflectances is calculated for the whole mission. A fourth order polynomial fit to these time-series is the basis for the empirical PMD degradation correction, which is calculated separately for GOME-2A and GOME-2B. The reference time is set to 1 February 2007 and 1 January 2013, respectively.

This corrected reflectance is translated into normalized rg-color space via the relation:

$$r = \frac{\rho(x,y,\lambda_R)}{\sum_{i=R,G,B}\rho(x,y,\lambda_i)}, g = \frac{\rho(x,y,\lambda_G)}{\sum_{i=R,G,B}\rho(x,y,\lambda_i)}. \tag{32}$$

with R in [569-804 nm], G in [400-557 nm] and B in [322-384 nm]. If M is the set of n normalized multi-temporal measurements over the same location (x,y), then a cloud-free (or minimum cloudiness) pixel rg_{CF} in M is selected with the brightness criterion $\|rg_{CF} - w\| \geq \|rg_k - w\|$ for $k = 1,..,n$, where $w = (1/3,1/3)$ is the *white point* in the rg chromaticity diagram. A global cloud-free composite is constructed by merging cloud-free reflectances $\rho_{CF}(\lambda)$ (corresponding to rg_{CF}) at all locations. Global cloud-free composites are constructed for each month of the year and are based on GOME-2A data from April 2008 until June 2013. These composites are also used for GOME-2B, because the GOME-2B mission lifetime is yet too short to construct global maps based on GOME-2B data. The effective cloud fraction is determined by examining separations between measured reflectances and their cloud-free composite values:

$$c_f = \min\left\{1, \sqrt{\sum_{i=R,G,B}\alpha(\lambda_i)\cdot\max\{0,[\rho(\lambda_i)-\rho_{CF}(\lambda_i)-\beta(\lambda_i)]\}^2}\right\}. \tag{33}$$

Scaling factors α determine a threshold for the fully cloudy scene and ensure that the cloud fraction is mapped to [0,1], while offsets β determine a threshold for a cloud-free scene and account for aerosol, shadow effects and other radiative effects. A fixed scaling factor and offset for each color is determined for GOME-2A and GOME-2B individually via histogram analysis.

OCRA has been given an additional algorithm for the proper discrimination between clouds and Sun-glint - most of the GOME-2 orbits are affected by this phenomenon, which can occur over water on the east side of the swath if a certain geometrical condition determined by the solar- and satellite zenith and -azimuth angles is fulfilled. If this is the case, OCRA raises a flag of possible sun-glint. For those measurements possibly affected by sun-glint, an attempt to distinguish between clouds and sun-glint is performed via three quantities: (1) a reflectance ratio (PMD4/PMD3, 0-based counting), (2) the Stokes fraction (PMD12, 0-based counting) and (3) a reflectance ratio (OCRA color R / OCRA color B). Thresholds for (1), (2) and (3) are determined empirically for both sensors, GOME-2A and GOME-2B. Currently, there are three sets of thresholds: one set for GOME-2A data before 11 March 2008 (with the old PMD Def 1.0), one set for GOME-2A data after 11 March 2008 (with the new PMD Def 3.1) and one set for the GOME-2B data. Evaluation of the three quantities against their corresponding thresholds determines if a measurement is to be considered as affected by Sun-glint or not. In the former case, the cloud fraction is set to zero (with an additional flag, stating that a Sun-glint correction has been performed), in the latter case the original cloud fraction is kept.

9.2 ROCINN cloud-top height and albedo algorithm

ROCINN (Loyola, 2004) is an algorithm based on O_2 A band reflectances from GOME: it delivers cloud-top height and cloud-top albedo. The independent pixel approximation is used; the cloud fraction c_f derived from the OCRA algorithm is taken as a fixed input to the ROCINN algorithm. In the simulations, only attenuation through oxygen absorption and molecular (Rayleigh) scattering of the direct solar beam and its reflection from ground or cloud-top is considered. Extinction by aerosols and by clouds is neglected, as is absorption by oxygen and Rayleigh scattering within and below any clouds. Surfaces are assumed to be Lambertian reflectors. In this approximation, we need only simulate reflectances along two photon paths through the atmosphere, leading to the total measured reflectance:

$$R_{sim}(\lambda) = c_f \langle R(\lambda, \Theta, c_a, c_z) \rangle + (1 - c_f) \langle R(\lambda, \Theta, s_a, s_z) \rangle \tag{34}$$

Here, $\langle R \rangle$ denotes the convoluted reflectance down to cloud-top or surface for path geometry Θ (solar zenith angle, viewing zenith angle and relative azimuth angle), wavelength λ, surface albedo s_a and cloud-top albedo c_a, and lower boundary heights s_z (surface) and c_z (cloud-top). Line-by-line transmittances must first be calculated using line spectroscopic information for the O_2 A band (taken from the HITRAN database), before convolution with the GOME-2 slit function. Quantities s_z and s_a are the surface height and albedo, taken from a suitable database and assumed known. The quantity s_a is taken from the MERIS black-sky albedo climatology (Popp et al. 2011). ROCINN aims to retrieve cloud-top height c_z and the cloud-top albedo c_a. Reflectance calculations based on Eq. (34) are used to create a complete data set of simulated reflectances for all viewing geometries and geophysical scenarios, as well as any combination of cloud fraction, cloud-top height and cloud-top albedo. High-resolution reflectances are computed with VLIDORT [Spurr, 2006] in vector mode for the range 758-772 nm at resolution 0.002 nm before convolution. The inversion of Eq. (34) is performed using neural network techniques.

9.3 Cloud-top pressure and cloud optical thickness calculation

The cloud-top pressure for GOME scenes is derived from the cloud-top height provided by ROCINN and an appropriated pressure profile.

Cloud reflectivity is calculated with the libRadtran radiative transfer package by Mayer and Kylling (2005), as a function of cloud optical thickness, surface albedo, solar zenith angle, and viewing zenith and azimuth. An effective radius of 10 micron is assumed and the cloud is placed between 1 and 10 km. The midlatitude summer atmosphere is assumed as background atmosphere to include Rayleigh scattering. Cloud single scattering properties for 760 nm are calculated with Mie theory and the

radiative transfer is solved with the plane-parallel discrete ordinate solver DISORT (Stamnes et al., 1988).

The cloud optical depth dependency on the cloud height is very small, for that reason a look-up table is created running libRadtran for a fixed cloud-top height of 4 km. A neural network is trained with this look-up table and the inverse problem is solved using the technique described in Loyola (2006). Cloud optical thickness τ is computed as a function of c_a cloud-top albedo, s_a the surface albedo, θ_0 the solar zenith angle, θ the satellite zenith angle, and ϕ the relative azimuth angle:

$$\tau = INV_{NN}(c_a, s_a, \theta_0, \theta, \phi) \tag{35}$$

The cloud optical thickness is computed using Eq. (35) taking as input the cloud-top albedo retrieved with ROCINN. For more details see Loyola et al. (2009).

9.4 Accounting for spatial-aliasing

The geolocation of a GOME-2 ground pixel is given for the location at the beginning of the detector read-out. Since the read-out of the detector takes some time and the satellite keeps moving during that time, different parts of the detector (i.e. different fitting windows) see slightly different geolocations. The integration time for the ground pixel is 187.5 ms and the read-out time for the full FPA-detector is 46.875 ms (i.e. 25% of the FPA integration time). The integration time for a PMD Pixel is 23.4375 ms (1/8 of a Ground Pixel) and the read-out time for the PMD-detector is 11.72 ms (i.e. 50% of the PMD integration time). Detectors can be read out from long-to-short wavelengths (sequence down) or from short-to-long wavelengths (sequence up). Since OCRA uses almost the full range of PMDs, we assume a mean time shift of 5 ms resulting in a mean spatial aliasing of ca. 2-3 km w.r.t to the geolocation given in the level 1 product. Here we also assume that the geolocation shifts linearly with time. The wavelength range of the O_2 A fitting window (758-771nm) results in a mean time shift of 7.4 ms (ca. 3 km). We note that this spatial aliasing of the O_2 A band, which is used by ROCINN to retrieve cloud-top height and albedo is almost identical to the spatial aliasing of the PMD-based OCRA cloud fraction, which serves as an a priori input for ROCINN. This is important because it assures that the geolocation for all cloud parameter is consistent.

The OCRA/ROCINN cloud parameters are mainly used for the GOME-2 trace gas column retrieval, as described in Chap. 2-8. All trace gases are subject to a different spatial aliasing, in particular different to the one relevant for the cloud parameters. Hence, the cloud information will be valid for a geolocation slightly shifted compared to the geolocation valid for the trace gases. This effect can be up to 10 km depending on the trace gas fitting window.

REFERENCES

Aliwell, S. R., M. Van Roozendael, P. V. Johnston, A. Richter, T. Wagner, D. W. Arlander, J. P. Burrows, D. J. Fish, R. L. Jones, K. K. Tørnkvist, J.-C. Lambert, K. Pfeilsticker, and I. Pundt (2002), Analysis for BrO in zenith-sky spectra: An intercomparison exercise for analysis improvement, J. Geophys. Res., 107, D14, doi: 10.1029/2001JD000329.

Balis, D., M. Koukouli, D. Loyola, P. Valks and N. Hao (2009), Validation report of GOME-2 total ozone products (OTO/O3, NTO/O3) processed with GDP 4.2, SAF/O3M/AUTH/GOME-2VAL/RP/03.

Balis, D., M. Koukouli, E. Zyrichidou, P. Valks and N. Hao (2013), Validation report of GOME-2/MetOp –B total ozone products (OTO/O3, NTO/O3) processed with GDP 4.7, SAF/O3M/AUTH/VR/O3.

Bhartia, P. K. (2003), Algorithm Theoretical Baseline Document, TOMS v8 Total ozone algorithm, NASA.

Bodhaine, B., N. Wood, E. Dutton, and J. Slusser (1999), On Rayleigh optical depth calculations, *J. Atmos. Ocean. Tech.*, 16, 1854-186.

Boersma K.F., H.J. Eskes and E.J. Brinksma (2004), Error analysis for tropospheric NO_2 retrieval from space, J. Geophys. Res., 109, D04311, doi:10.1029/2003JD003962.

Bogumil, K., Orphal, J., Homann, T. Voigt, S., Spietz, P., Fleischmann, O. C., Vogel, A., Hartmann, M., Bovensmann, H., Frerik, J., and J.P. Burrows (2003), Measurements of Molecular Absorption Spectra with the SCIAMACHY Pre-Flight Model: Instrument Characterization and Reference Data for Atmospheric Remote-Sensing in the 230-2380 nm Region, J.Photochem. Photobiol. A.,157, 167-184.

Brenot, H.; Theys, N.; Clarisse, L.; van Geffen, J.; van Gent, J.; Van Roozendael, M.; van der A, R.; Hurtmans, D.; Coheur, P.-F.; Clerbaux, C.; Valks, P.; Hedelt, P.; Prata, F.; Rasson, O.; Sievers, K.; Zehner, C. (2014), Support to Aviation Control Service (SACS): an online service for near-real-time satellite monitoring of volcanic plumes, Natural Hazards and Earth System Science, Volume 14, Issue 5, 2014, pp.1099-1123

Brion, J., Chakir, A., Charbonnier, J., Daumont, D., Parisse, C. and Malicet, J. (1998), Absorption spectra measurements for the ozone molecule in the 350-830 nm region, J. Atmos. Chem., 30, 291-299.

Bruns M., H. Bovensmann, A. Richter, and J.P. Burrows (2003), A Stratospheric BrO climatology for the GOME-2 instrument, O3M-SAF Visiting Scientist Report, IUP University of Bremen, Feb. 2003.

Burrows J.P., M. Weber, M. Buchwitz, V.V. Rozanov, A. Ladstaetter-Weissenmeyer, A. Richter, R. de Beek, R. Hoogen, K. Bramstadt, K.-U. Eichmann, M. Eisinger and D. Perner (1999a), The Global Ozone Monitoring Experiment (GOME): mission concept and first scientific results, *J. Atmos. Sci*, 56, 151-175.

Burrows, J.P., A. Richter, A. Dehn, B. Deters, S. Himmelmann, S. Voigt, J. Orphal (1999b), Atmospheric remote-sensing reference data from GOME - 2. Temperature-dependent absorption cross-sections of O_3 in the 231-794 nm range. J. Quant. Spectrosc. Radiat. Transfer, 61, 509-517.

Chance, K., and R. Spurr (1997), Ring effect studies: Rayleigh scattering including molecular parameters for rotational Raman scattering, and the Fraunhofer spectrum, Applied Optics, 36, 5224-5230.

Chance, K., and Kurucz, R. L. (2010), An improved high-resolution solar reference spectrum for earth's atmosphere measurements in the ultraviolet, visible and near infrared, J.Quant. Spectrosc. Ra.,111, 1289-1295.

Chehade, W., et al., (2013), Temperature dependent ozone absorption cross section spectra measured with the GOME-2 FM3 spectrometer and first application in satellite retrievals, Atmos. Meas. Tech., 6, 1623-1632.

De Smedt, I., Van Roozendael, M., Stavrakou, T., Müller, J.-F., Lerot, C., Theys, N., Valks, P., Hao, N., and van der A, R. (2012): Improved retrieval of global tropospheric formaldehyde columns from GOME-2/MetOp-A addressing noise reduction and instrumental degradation issues, Atmos. Meas. Tech., 5, 2933-2949, doi:10.5194/amt-5-2933-2012.

De Smedt, I., G. Pinardi, M. Van Roozendael, N. Hao and P. Valks (2013), Interim verification of GOME-2 GDP 4.7 HCHO column data for MetOp-B – ORR, SAF/O3M/IASB/ORR/HCHO, May 2013.

De Smedt, I., G. Pinardi, H. Yu, F. Hendrick, C. Gielen, N. Hao, M. Begoin and P. Valks (2015), O3M SAF Validation Report for GOME-2 GDP 4.8 HCHO column data, SAF/O3M/IASB/VR/HCHO/113, Issue 1/1, Oct, 2015.

Eskes, H.J., K. F. Boersma (2003), Averaging kernels for DOAS total-column satellite retrievals, Atmos. Chem. Phys., 3, 1285-1291.

EUMETSAT (2011), GOME-2 Products Guide, Ref.: EUM/OPS-EPS/MAN/07/0445, Issue: v3, Date: 17 Mar 2011.

Fortuin, J.P.F., and H. Kelder (1998), An ozone climatology based on ozonesonde and satellite measurements, J. Geophys. Res., 103, 31709-31734.

Fleischmann, O. C., Hartmann, M., Burrows, J. P. , Orphal, J., (2004), New ultraviolet absorption cross-sections of BrO at atmospheric temperatures measured by time-windowing Fourier transform spectroscopy, J. photochem. photobiol., A Chem., 168, no1-2, 117-132.

Grainger, J.F., and J. Ring (1962), Anomalous Fraunhofer Line Profiles, Nature, 193, 762.

Greenblatt, G.D., J.J. Orlando, J.B. Burkholder, and A.R. Ravishankara (1990), Absorption measurements of oxygen between 330 and 1140 nm, *J. Geophys. Res.*, 95, 18577-18582.

Grossi, M., Valks, P., Loyola, D., Aberle, B., Slijkhuis, S., Wagner, T., Beirle, S., and Lang, R.: Total column water vapour measurements from GOME-2 MetOp-A and MetOp-B, Atmos. Meas. Tech., 8, 1111-1133, doi:10.5194/amt-8-1111-2015, 2015.

Grossi, M., N. Kalakoski, and P. Valks (2015), O3M SAF Validation Report for GOME-2 GDP 4.8 H_2O column data, SAF/O3M/DLR/ORR/H2O, Issue 10/2015, Oct, 2015.

Grzegorski, M. (2009), Cloud retrieval from UV/VIS satellite instruments (SCIAMACHY and GOME), PhD thesis, University of Heidelberg

Gür, B., P. Spietz, J. Orphal and J. Burrows (2005), Absorption Spectra Measurements with the GOME-2 FMs using the IUP/IFE-UB´s Calibration Apparatus for Trace Gas Absorption Spectroscopy CATGAS, Final Report, IUP University of Bremen, Oct. 2005.

Hao, N., M. E. Koukouli, A. Inness, P. Valks, D. G. Loyola, W. Zimmer, D. S. Balis, I. Zyrichidou, M. Van Roozendael, C. Lerot, and R. J. D. Spurr (2014), GOME-2 total ozone columns from MetOp-A/MetOp-B and assimilation in the MACC system, Atmos. Meas. Tech., 7, 2937-2951, doi: 10.5194/amt-7-2937-2014.

Herman, J.R, and E.A. Celarier (1997), Earth surface reflectivity climatology at 340 nm to 380 nm from TOMS data, J. Geophys. Res., 102, 28003-28011.

Horowitz, L., Walters, S., Mauzerall, D., Emmons, L., Rasch, P., Granier, C., Tie, X., Lamarque, J., Schultz, M., Tyndall, G., Orlando, J., and Brasseur, G. (2003), A global simulation of tropospheric ozone and related tracers: description and evaluation of MOZART, version 2, J. Geophys. Res., 108(D24), 4784, doi:10.1029/2002JD002853.

Kalakoski, N., M. Grossi and P. Valks (2013), Interim verification report of GOME-2 GDP 4.7 H_2O column data for MetOp-B, ORR,, SAF/O3M/FMI/ORR/H2O, May 2013.

Kalakoski, N., Kujanpää, J., Sofieva, V., Tamminen, J., Grossi, M., and Valks, P.: Comparison of GOME-2/Metop total column water vapour with ground-based and in situ measurements, Atmos. Meas. Tech. Discuss., 7, 12517-12543, doi:10.5194/amtd-7-12517-2014, 2014.

Koelemeijer, R.B.A., J.F. de Haan, and P. Stammes (2003), A database of spectral surface reflectivity in the range 335--772 nm derived from 5.5 years of GOME observations, J. Geophys. Res., 108, 4070, doi:10.1029/2002JD0024.

Kneizys F.X., E.P. Shettle, L.W. Abreu, J.H. Chetwynd, G.P. Anderson, W.O. Gallery, J.E.A. Selby, and S.A. Clough (1988), Users Guide to LOWTRAN 7, Air Force Geophysics Laboratory, Environmental Research Papers, No. 1010, AFGL-TR-88-0177.

Khokhar, M. F., Frankenberg, C., Beirle, S., Kühl, S., Van Roozendael, M., Richter, A., Platt U., and Wagner, T. (2005), Satellite observations of atmospheric SO2 from volcanic eruptions during the time period of 1996 to 2002, J. Adv. Space Res., 36(5), 879–887, doi:10.1016/j.asr.2005.04.114.

Koukouli, M. E., Balis, D. S., Loyola, D., Valks, P., Zimmer, W., Hao, N., Lambert, J.-C., Van Roozendael, M., Lerot, C., and Spurr, R. J. D. (2012), Geophysical validation and long-term consistency between GOME-2/MetOp-A total ozone column and measurements from the sensors GOME/ERS-2, SCIAMACHY/ENVISAT and OMI/Aura, Atmos. Meas. Tech., 5, 2169-2181, doi:10.5194/amt-5-2169-2012.

Koukouli, M., E. Zyrichidou, D. Balis, P. Valks and N. Hao (2015), Validation report of GOME-2 total ozone products processed with GDP 4.8, SAF/O3M/AUTH/VRR/O3, Issue 1/0, Dec. 2015.

Lambert, J.-C., and J. Granville, Harmonic climatology of stratospheric NO_2, BIRA-IASB, Brussels, 2004.

Lambert, J.-C., I. De Smedt, J. Granville, and P. Valks (2007), Initial validation of GOME-2 Nitrogen Dioxide columns (GDP 4.2 OTO/NO2 and NTO/NO2): March – June 2007, TN-IASB-GOME2-O3MSAF-NO-01-1/A.

Lambert, J.-C., G. Pinardi, J. Granville, K. Clemer, A. Delcloo, P. Valks and N. Hao (2011), GOME-2 GDP 4.3 / 4.4 total NO_2 and tropospheric NO_2 (NTO/OTO) validation: 2007-2010, TN-IASB-GOME2-O3MSAF-NO2-v4-2011.

Liu, X., M. Newchurch, R. Loughman, and P.K. Bhartia (2004), Errors resulting from assuming opaque Lambertian clouds in TOMS ozone retrieval, Journal of Quantitative Spectroscopy and Radiative Transfer, 85, 337-365.

Loyola, D., and T. Ruppert (1998), A new PMD cloud-recognition algorithm for GOME, ESA Earth Observation Quarterly, 58, 45-47.

Loyola, D. (2004), Automatic Cloud Analysis from Polar-Orbiting Satellites using Neural Network and Data Fusion Techniques, IEEE International Geoscience and Remote Sensing Symposium, 4, 2530-2534, Alaska.

Loyola D. (2006), "Applications of Neural Network Methods to the Processing of Earth Observation Satellite Data", Neural Networks, vol. 19, no. 2, pp. 168-177.

Loyola D., Thomas W., Livschitz Y., Ruppert T., Albert P.,and Hollmann R. (2007), Cloud properties derived from GOME/ERS-2 backscatter data for trace gas retrieval, IEEE Transactions in Geoscience and Remote Sensing, vol. 45, no. 9, pp. 2747-2758.

Loyola, D. (2007), A semi-transparent Lambertian cloud model for ozone retrieval, DLR presentation, September 2007.

Loyola D., Thomas W., Spurr, R., B. Mayer (2009), Global patterns in daytime cloud properties derived from GOME backscatter UV-VIS measurements, International Journal of Remote Sensing, in press.

Loyola D., Koukouli M. E., Valks P., Balis D. S., Hao N., Van Roozendael M., Spurr R. J. D., Zimmer W., Kiemle S., Lerot C., Lambert J.-C (2011), The GOME-2 total column ozone product: Retrieval algorithm and ground-based validation, Journal of Geophysical Research, vol. 116, D07302.

Lutz, R., Loyola, D., Gimeno García, S., and Romahn, F.: OCRA radiometric cloud fractions for GOME-2 on MetOp-A/B, Atmos. Meas. Tech., 9, 2357-2379, doi:10.5194/amt-9-2357-2016, 2016.

Malicet, J., D. Daumont, J. Charbonnier, C. Parisse, A. Chakir, and J. Brion (1995), Ozone UV spectroscopy. II. Absorption cross-sections and temperature dependence, J. Atmos. Chem., 21, 263-273.

Mayer, B., and A. Kylling (2005), Technical note: The libRadtran software package for radiative transfer calculations - description and examples of use, Atmos. Chem. Phys., vol. 5, pp. 1855-1877.

Meller, R., and G. K. Moortgat (2000), Temperature dependence of the absorption cross sections of formaldehyde between 223 and 323 K in the wavelength range 225–375 nm, J. Geophys. Res., 105(D6), 7089–7101, doi:10.1029/1999JD901074.

Müller, J.-F. and Stavrakou, T. (2005): Inversion of CO and NO_x emissions using the adjoint of the IMAGES model, Atmos. Chem. Phys., 5, 1157-1186, doi:10.5194/acp-5-1157-2005.

Munro, R., Eisinger, M., Anderson, C., Callies, J., Corpaccioli, E., Lang, R., Lefebvre, A., Livschitz, Y., and Albinana, A. P. (2006), GOME-2 on MetOp, Proc. of The 2006 EUMETSAT Meteorological Satellite Conference, Helsinki, Finland.

Noël, S., Buchwitz, M., Bovensmann, H., Hoogen, R., Burrows, J. P. (1999), Atmospheric Water Vapor Amounts Retrievd from GOME Satellite data, Geophys. Res. Lett., 26, 1841-1844.

Nüß, H., A. Richter, P. Valks and J. Burrows (2006), Improvement of the NO_2 total column retrieval for GOME-2, O3M SAF Visiting Scientist Activity, Final Report, IUP University of Bremen, Oct. 2006.

Pinardi, G., Lambert, J.-C., Y. Huan, I. De Smedt, J. Granville, M. Van Roozendael and P. Valks (2013), Interim verification report of GOME-2 GDP 4.7 NO_2 column data for MetOp-B, ORR, SAF/O3M/IASB/VR/NO2.

Pinardi, G., Lambert, J.-C., Y. Huan, I. De Smedt, J. Granville, M. Van Roozendael and P. Valks (2015), O3M SAF Validation report of GOME-2 GDP 4.8 NO_2 column data, SAF/O3M/IASB/VR/NO2, Issue 1/0, Oct. 2015.

Pinardi, G., M. Van Roozendael, F. Hendrick and P. Valks (2017), AC SAF Validation report of GOME-2 GDP 4.8 OClO slant column data record, SAF/AC/IASB/VR/OClO, Issue 1/1, June 2017.

Popp, C., Wang, P., Brunner, D., Stammes, P., Zhou, Y., and Grzegorski, M., MERIS albedo climatology for FRESCO+ O2 A-band cloud retrieval, Atmos. Meas. Tech., 4, 463-483, 2011.

Puķīte,J., S. Kühl, T. Deutschmann, U. Platt, and T. Wagner (2010), Extending differential optical absorption spectroscopy for limb measurements in the UV, Atmos. Meas. Tech., 3, 631-653.

Richter, A , F. Wittrock, M. Eisinger and J. P. Burrows (1998), GOME observations of tropospheric BrO in Northern Hemispheric spring and summer 1997, Geophys. Res. Lett., No. 25, pp. 2683-2686.

Richter, A., and J. Burrows (2002), Tropospheric NO_2 from GOME measurements, Adv. Space Res., 29, 1673-1683.

Richter, A., Wittrock, F., Ladstätter-Weissenmayer, A., and Burrows, J. P. (2002), GOME measurements of stratospheric and tropospheric BrO, Adv. Space Res., 29, 1667-1672.

Rix M., Valks P., Hao N., van Geffen J., Clerbaux C., Clarisse L., Coheur P.-F., Loyola D., Erbertseder T., Zimmer W., and Emmadi S. (2009), Satellite Monitoring of Volcanic Sulfur Dioxide Emissions for Early Warning of Volcanic Hazards, IEEE Journal of Selected Topics in Applied Earth Observations and Remote Sensing, vol. 2, no. 3, pp. 196-2006, 2009.

Rix, M., P. Valks, N. Hao, D. Loyola, H. Schlager, H. Huntrieser, J. Flemming, U. Koehler, U. Schumann, A. Inness (2012), Volcanic SO2, BrO and plume height estimations using GOME-2 satellite measurements during the eruption of Eyjafjallajökull in May 2010, J. Geophys. Res., 117, D00U19, doi:10.1029/2011JD016718.

Rothman, L., et al. (2003), The HITRAN molecular spectroscopic database: edition of 2000 including updates through 2001, , J. Quant. Spectrosc. Rad. Transfer, 82, 5-44.

Rothman, L.S., et al.(2005): The HITRAN 2004 molecular spectroscopic database, J. Quant. Spectr. Rad. Transfer 96, 139-204, 2005

Rozanov, A., Rozanov, V., and Burrows, J. P. (2001), A numerical radiative transfer model for a spherical planetary atmosphere: Combined differential integral approach involving the Piccard iterative approximation, J. Quant. Spectrosc. Radiat. Transfer, 69, 491–512.

Siddans, R., B.J. Kerridge, B.G. Latter, J. Smeets and G. Otter (2006), Analysis of GOME-2 Slit function measurements, Algorithm Theoretical Basis Document, EUM/CO/04/1298/RM.

Spurr, R. J. D., T. P. Kurosu, and K. V. Chance (2001), A Linearized discrete Ordinate Radiative Transfer Model for Atmospheric Remote Sensing Retrieval, J. Quant. Spectrosc. Radiat. Transfer, 68, 689-735.

Spurr, R. (2003), LIDORT V2PLUS: a comprehensive radiative transfer package for nadir viewing spectrometers, remote Sensing of clouds and atmosphere, Proceedings SPIE conference 5235, Barcelona, Spain.

Spurr R.J.D., Van Roozendael M., Loyola D.G. (2004), "Algorithm Theoretical Basis Document for GOME Total Column Densities of Ozone and Nitrogen Dioxide. P/GDOAS: GDP 4.0", ERSE-DTEX-EOPG-TN-04-0007, Iss./Rev.:1/A.

Spurr R.J.D., D. Loyola, W. Thomas, W. Balzer, E. Mikusch, B. Aberle, S. Slijkhuis, T. Ruppert, M. Van Roozendael, J.-C. Lambert, and T. V. Soebijanta (2005), GOME Level 1-to-2 Data Processor Version 3.0: A Major Upgrade of the GOME/ERS-2 Total Ozone Retrieval Algorithm, Applied Optics, 44, 7196-7209.

Spurr R.J.D., (2006), VLIDORT : A linearized pseudo-spherical vector discrete ordinate radiative transfer code for forward model and retrieval studies in multilayer multiple scattering media, Journal of Quantitative Spectroscopy & Radiative Transfer, vol. 102, no. 2, pp. 316-342.

Spurr, R. (2008), LIDORT and VLIDORT: Linearized pseudo-spherical scalar and vector discrete ordinate radiative transfer models for use in remote sensing retrieval problems, in Light Scattering Reviews, vol. 3, edited by A. Kokhanovsky, 229-275, doi:10.1007/978-3-540- 48546-97, Springer, Berlin.

Spurr, R. et al. (2010), GOME-2 trace gas column retrievals: optimized wavelengths for the O3 AMF, Final Report, O3MSAF-VS project.

Stamnes, K. and Tsay, S.C. and Wiscombe, W. and Jayaweera, K (1988), A numerically stable algorithm for discrete-ordinate-method radiative transfer in multiple scattering and emitting layered media, Applied Optics, vol. 27,nr. 12, 2502-2509.

Taubman,B.F., Hains, J.C., Thompson, A.M., Marufu L.T., Doddridge, B.G., Stehr, J.W., Piety, J.A., and Dickerson, R.R. (2006), Aircraft vertical profiles of trace gas and aerosol pollution over the mid-Atlantic United States: Statistics and meteorological cluster analysis, J. Geophys. Res., 111, D10S07.

Theys, N., Van Roozendael, M., Hendrick, F., Yang, X., De Smedt, I., Richter, A., Begoin, M., Errera, Q., Johnston, P. V., Kreher, K., and De Mazière, M. (2011), Global observations of tropospheric BrO columns using GOME-2 satellite data, Atmos. Chem. Phys., 11, 1791-1811.

Theys, N., F. Hendrick, M. Van Roozedael, N. Hao and P. Valks (2013a), Interim verification report of GOME-2 GDP 4.7 BrO column data for MetOp-B, ORR, SAF/O3M/IASB/ORR/BRO.

Theys, N., J. van Gent, M. Van Roozedael, M. Koukouli, D. Balis, P. Hedelt and P. Valks (2013b), Interim verification report of GOME-2 GDP 4.7 SO_2 column data for MetOp-B, ORR, SAF/O3M/IASB/ORR/SO2.

Theys, N., F. Hendrick, J. van Gent, M. Van Roozedael, N. Hao and P. Valks (2015a), O3M SAF validation report of GOME-2 GDP 4.8 Total BrO column data, SAF/O3M/BIRA/VR/BRO, Issue 1/1, Oct. 2015.

Theys, N., M. Koukouli, G. Pinardi, M. Van Roozedael, D. Balis, P. Hedelt and P. Valks (2015b), O3M SAF validation report of GOME-2 GDP 4.8 Total SO_2 column data, SAF/O3M/IASB/VR/SO2/112, Issue 1/1, Dec. 2015.

Thomas, W., Erbertseder, T., Ruppert, T., van Roozendael, M., Verdebout, J., Meleti, C., Balis, D., Zerefos, C. (2005), On the retrieval of Volcanic Sulfur Dioxide Emissions from GOME backscatter measurements, *J. Atm. Chem.*, 50, 295-320.

Valks P., Pinardi G., Richter A., Lambert J.-C., Hao N., Loyola D., Van Roozendael M., Emmadi S. (2011), Operational total and tropospheric NO2 column retrieval for GOME-2, Atmospheric Measurement Techniques, vol. 4, pp. 1491-1514.

Valks, P., et al., (2017), Product User Manual for GOME Total Column Products of Ozone, NO_2, BrO, HCHO, SO_2, H_2O, OClO and Cloud Properties, GDP 4.8, SAF/AC/DLR/PUM/01, Iss. 3/A, Rev. 2, June, 2017.

Vandaele, A. C., C. Hermans, S. Fally, M. Carleer, R. Colin, M.-F. Merienne, A. Jenouvrier, and B. Coquart (2002), High-resolution Fourier transform measurement of the NO2 visible and near-infrared absorption cross section: Temperature and pressure effects, J. Geophys. Res., 107(D18), 4348, doi:10.1029/2001JD000971.

Van Roozendael, M., V. Soebijanta, C. Fayt, and J.-C. Lambert (2002), Investigation of DOAS Issues Affecting the Accuracy of the GDP Version 3.0 Total Ozone Product, in ERS-2 GOME GDP 3.0 Implementation and Delta Validation, Ed. J.-C. Lambert, ERSE-DTEX-EOAD-TN-02-0006, ESA/ESRIN, Frascati, Italy, Chap.6, pp.97-129.

Van Roozendael, M., and R.J.D. Spurr (2003), GOME Direct Fitting (GODFIT) Validation Report, ERS Exploitation AO/1-4235/02/I-LG.

Van Roozendael, M., J.-C. Lambert, R. J. D. Spurr, and C. Fayt (2004), GOME Direct Fitting (GODFIT) GDOAS Delta Validation Report, ERS Exploitation AO/1-4235/02/I-LG.

Van Roozedael, M., D. Loyola, R. Spurr, D. Balis, J.-C. Lambert, Y. Livschitz, P. Valks, T. Ruppert, P. Kenter, C. Fayt, and C. Zehner (2006), Ten years of GOME/ERS-2 total ozone data - The new GOME Data Processor (GDP) Version 4.0: I. Algorithm Description, J. Geophys. Res. 111, D14311, 10.1029/2005JD006375.

Wagner, T., J.Heland, M. Zoeger, U. Platt (2003), A fast H_2O total column density product from GOME-Validation with in-situ aircraft measurements, Atmos. Chem. Phys., 3, 651-663.

Wagner T., S. Beirle, M. Grzegorski, U. Platt (2006), Global trends (1996–2003) of total column precipitable water observed by Global Ozone Monitoring Experiment (GOME) on ERS-2 and their relation to near-surface temperature, J. Geophys. Res., 111, D12102, doi:10.1029/2005JD006523